

1 **Ancient origin of the rod bipolar cell pathway in the vertebrate retina**

2

3 Ayana M Hellevik^{1,*}, Philip Mardoum^{1,*}, Joshua Hahn^{2,*}, Yvonne Kölsch^{3,4}, Florence D D’Orazi¹,
4 Sachihiro C. Suzuki¹, Leanne Godinho⁵, Owen Lawrence¹, Fred Rieke^{6,7}, Karthik Shekhar^{2,8},
5 Joshua R Sanes³, Herwig Baier⁴, Tom Baden^{9,10}, Rachel O Wong¹, Takeshi Yoshimatsu^{11,12,#}

6

7 1, Department of Biological Structure, University of Washington, Seattle, WA 98195, USA; 2,
8 Department of Chemical and Biomolecular Engineering; Helen Wills Neuroscience Institute;
9 Vision Sciences Graduate Program; California Institute of Quantitative Biosciences (QB3),
10 University of California Berkley, Berkeley, CA 94720, USA; 3, Department of Molecular & Cellular
11 Biology and Center for Brain Science, Harvard University, Cambridge, MA 02138, USA; 4, Max
12 Planck Institute for Biological Intelligence, Department Genes – Circuits – Behavior, 82152
13 Martinsried, Germany; 5, Institute of Neuronal Cell Biology, Technische Universität München,
14 80802 Munich, Germany; 6, Department of Physiology and Biophysics, University of Washington,
15 Seattle, WA 98195, USA; 7, Vision Science Center, University of Washington, Seattle, WA 98195,
16 USA; 8, Biological Systems and Engineering Division, Lawrence Berkeley National Laboratory,
17 Berkeley, CA 94720, USA; 9, School of Life Sciences, University of Sussex, Brighton, BN1 9QG,
18 UK; 10, Institute of Ophthalmic Research, University of Tübingen, Tübingen, 72076, Germany;
19 11, Department of Ophthalmology & Visual Sciences, Washington University in St Louis School
20 of Medicine, St Louis, MO 63110, USA; 12, BioRTC, Yobe State University, Damatsuru, Yobe
21 620101, Nigeria

22

23 *These authors contributed equally to this study

24 #Lead contact: Takeshi Yoshimatsu takeshi@wustl.edu

25

26 **Keywords**

27 Rod, Rod bipolar cells, Retina, Evolution

28

29 **Highlights**

30 - Zebrafish have two rod bipolar cell types (RBC1/2).

31 - Synaptic connectivity of RBC1 resembles that of the mammalian RBCs.

32 - The primary rod pathway therefore probably evolved more than 400 million years ago.

33 - The second zebrafish RBC type, RBC2, forms a separate pathway from RBC1.

34

35 **ABSTRACT**

36 Vertebrates rely on rod photoreceptors for vision in low-light conditions¹. Mammals have a
37 specialized downstream circuit for rod signaling called the primary rod pathway, which comprises
38 specific cell types and wiring patterns that are thought to be unique to this lineage²⁻⁶. Thus, it has
39 been long assumed that the primary rod pathway evolved in mammals^{3,5-7}. Here, we challenge
40 this view by demonstrating that the mammalian primary rod pathway is conserved in zebrafish,
41 which diverged from extant mammals ~400 million years ago. Using single-cell RNA-sequencing,
42 we identified two bipolar cell (BC) types in zebrafish that are related to mammalian rod BCs
43 (RBCs) of the primary rod pathway. By combining electrophysiology, histology, and ultrastructural
44 reconstruction of the zebrafish RBCs, we found that, like mammalian RBCs⁸, both zebrafish RBC
45 types connect with all rods and red-cones in their dendritic territory, and provide output largely
46 onto amacrine cells. The wiring pattern of the amacrine cells post-synaptic to one RBC type is
47 strikingly similar to that of mammalian RBCs, suggesting that the cell types and circuit design of
48 the primary rod pathway have emerged before the divergence of teleost fish and amniotes
49 (mammals, birds, reptiles). The second RBC type in zebrafish, which forms separate pathways
50 from the first RBC type, is either lost in mammals or emerged in fish to serve yet unknown roles.

51

52 INTRODUCTION

53 Rod photoreceptors of the vertebrate retina are capable of detecting very dim light, down to
54 individual photons^{9–14}. The mammalian cell types and circuitry that convey rod-driven signals,
55 called the primary rod pathway, were identified and defined in the cat retina about 50 years ago¹⁵.
56 Since its initial characterization, this rod pathway has been examined extensively in many
57 mammalian species including in humans, where it consistently uses homologous cell types and
58 connectivity patterns: Rod bipolar cells (RBCs), as well as A2 and A17 amacrine cells^{3,5,6,16,17}. The
59 RBC is a molecularly, structurally and functionally distinct retinal bipolar cell type that receives
60 input from all rods within its dendritic field and is predominantly driven by rods^{8,18–21}. All other
61 bipolar cell types receive most of their photoreceptor input from cones, which operate in daylight
62 conditions. In contrast to mammals, the bipolar cells that have been characterized in non-
63 mammals lack clear distinctions regarding the ratio of rod and cone inputs^{14,22}. Thus, it is not
64 surprising that the RBC is thought to be unique to mammals, a notion that has led to the prevailing
65 view that the rod pathway evolved separately in this class^{3,5–7}. However, the molecular, structural
66 and functional signatures that together define bipolar cell types in mammals are largely unknown
67 in non-mammals, so it remains unclear whether the signatures characteristic of the mammalian
68 RBC and its downstream pathway are present in non-mammals. To address this issue, we
69 focused on zebrafish, a species that allows transgenic labeling of neuronal populations, to analyze
70 single-cell transcriptomics, histology, physiology and circuit reconstructions of genetically-defined
71 retinal bipolar cells.

72 There are more than a dozen BC types in mammals that are diverse in morphology, connectivity
73 and molecular profiles^{23–27}, but can be classified into two main groups: ON BCs that depolarize
74 and OFF BCs that hyperpolarize in response to increases in luminance²⁸. RBCs are one type of
75 ON BCs that are distinct in many ways from all other BCs, which mainly connect with cones and
76 are called cone BCs (CBCs) here. Transcriptionally, mammalian RBCs can be distinguished from

77 CBCs by the expression of protein kinase C-alpha (PKC α)²⁹. Morphologically, the axon terminals
78 of RBCs are generally larger than those of CBCs and end in the innermost layer of the inner
79 plexiform layer (IPL). The synaptic arrangement of the RBC axons differs from the common
80 synaptic arrangement of most cone bipolar cells. Whereas CBC axons directly synapse onto the
81 retinal output neurons, retinal ganglion cells (RGCs), along with a plethora of amacrine cells (ACs),
82 RBCs predominately form a 'dyadic' synapse with two types of inhibitory amacrine cells, small
83 field A2 (or A-II) and large-field A17 ACs^{15,18,19,30}. The A17 AC almost exclusively makes reciprocal
84 feedback synapses onto RBC axon terminals³¹. In contrast, A2 ACs receive numerous synapses
85 from RBCs (~40 synapses per RBC in mice), but do not provide feedback onto the RBCs^{18,32}.
86 These RBC to A2 AC synapses are the critical sites for the amplification and gain control of rod
87 signals^{33–35}. Rod signals are eventually relayed to RGCs by connections from A2 ACs on CBCs,
88 which split rod signals into ON and OFF channels via sign-conserving gap junctions with ON
89 CBCs and inhibitory synapses with OFF CBCs^{15,36,37}.

90 Here, by analyzing single-cell transcriptomic profiles of zebrafish BCs, we discovered two BC
91 types, RBC1 and RBC2, with molecular signatures similar to those of mammalian RBCs. Using
92 transgenic zebrafish lines that express a fluorescent protein in RBC1 or RBC2 cells, we identified
93 the inputs and outputs of RBC1 and RBC2. We found that both zebrafish RBC types connect with
94 all rods and red cones (or longwave-length sensitive, LWS, cones) inside their dendritic fields.
95 We further reconstructed the downstream circuits of both BC types using serial block-face
96 electron microscopy and found that RBC1 predominantly synapses onto three morphological
97 types of ACs. The circuit diagrams and synaptic arrangements of two of the ACs closely resemble
98 those of the mammalian A2 and A17 ACs. In contrast, RBC2 mainly connects to a different set of
99 ACs, which does not include A2-like ACs. These results suggest that (i) zebrafish possess two
100 separate pathways for processing rod signals, and that (ii) one of these is similar to the rod →
101 RBC → A2 AC → CBC → RGC pathway found in mammals. We conclude that the primary rod

102 pathway emerged >400 million years ago, before the divergence of teleosts and mammals in the
103 Devonian.

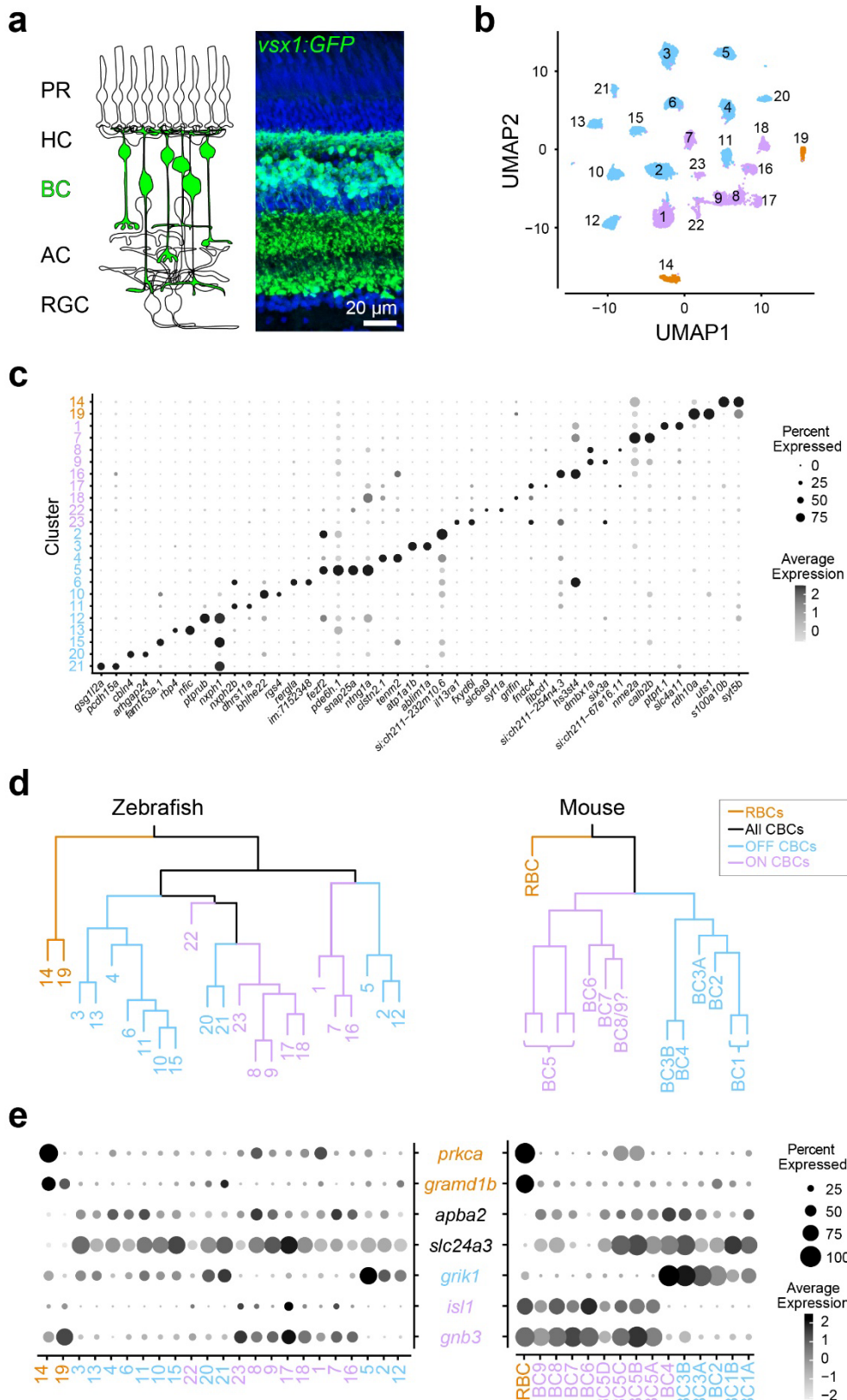
104

105 **RESULTS**

106 **Two zebrafish BC types are transcriptionally analogous to the mammalian RBCs**

107 We first determined the transcriptional similarity between each zebrafish BC type and the
108 mammalian RBCs by using single-cell RNA-sequencing (scRNA-seq) in adult zebrafish. BCs
109 were isolated using a fluorescent marker in the *Tg(vsx1:GFP)^{nns5}* transgenic line, in which all BCs
110 express GFP³⁸ (Fig. 1a). Clustering analysis of 19492 high-quality single cell transcriptomes
111 identified 23 molecularly distinct BC clusters (Fig. 1b,c). To identify the clusters most similar to
112 mammalian RBCs, we performed a hierarchical clustering analysis based on average
113 transcriptomic profiles (Fig. 1d) and combined this with the expression patterns of marker genes
114 identified in mice to tentatively annotate each cluster as ON CBC, OFF CBC or RBC (Fig. 1e; ²⁷).
115 In mice, RBCs are clearly separated from CBCs at the first dendrogram bifurcation²⁷. Similarly,
116 the first dendrogram bifurcation separates two BCs from the other BCs in zebrafish. In contrast to
117 mice, however, the zebrafish RBC clade contained two molecularly distinct clusters 14 (c14) and
118 19 (c19) (Fig. 1d). We observed that *prkca* (the gene encoding PKC α), a common marker of
119 mammalian RBCs, is only highly expressed in c14. However, both c14 and c19 specifically
120 express *gramd1b*, which is an RBC-specific marker in mice. In addition to these genetic
121 signatures similar to mammalian RBCs, both c14 and c19 clusters express neurotransmitter
122 receptor, *grm6a* and *grm6b*, and its downstream signaling molecules, *trpm1a*, *trpm1b*, *nyx* and
123 *rgs11*, which are essential for mediating rod inputs in mammals³⁹ (Fig. S1). Therefore, we
124 hypothesized that zebrafish, unlike mice, may possess two RBC types, which we call RBC1 (c14)
125 and RBC2 (c19).

Figure 1



127 **Figure 1. Comparison of single-cell gene expressions identified two possible rod bipolar
128 cells in zebrafish**

129 **a**, Schematic representation of retinal circuits (left) and an image of a retinal slice from
130 *Tg(vsx1:GFP)^{nns5}* transgenic adult zebrafish (right). GFP expression in all bipolar cells (BCs).
131 Nuclei was stained by DAPI. PR: photoreceptor, HC: horizontal cell, AC: amacrine cell, RGC:
132 retinal ganglion cell. **b**, 2D visualization of single-cell clusters using Uniform Manifold
133 Approximation (UMAP)⁴⁰. Individual points correspond to single cells colored according to cluster
134 identity. **c**, Marker genes for each cluster. **d**, Agglomerative hierarchical clustering of average
135 gene signatures of clusters using the correlation metric and complete linkage. BC subclasses
136 (colors) were assigned based on the known marker expressions shown in **e**. **e**, Gene expression
137 patterns of known BC subclass markers in BC clusters. The size of each circle depicts the
138 percentage of cells in the cluster in which the marker was detected (≥ 1 UMI), and its contrast
139 depicts the scaled average expression level of cells within the cluster in **c,e**. Data for mouse is
140 from Shekhar K, et al., 2016, Cell.

Figure S1

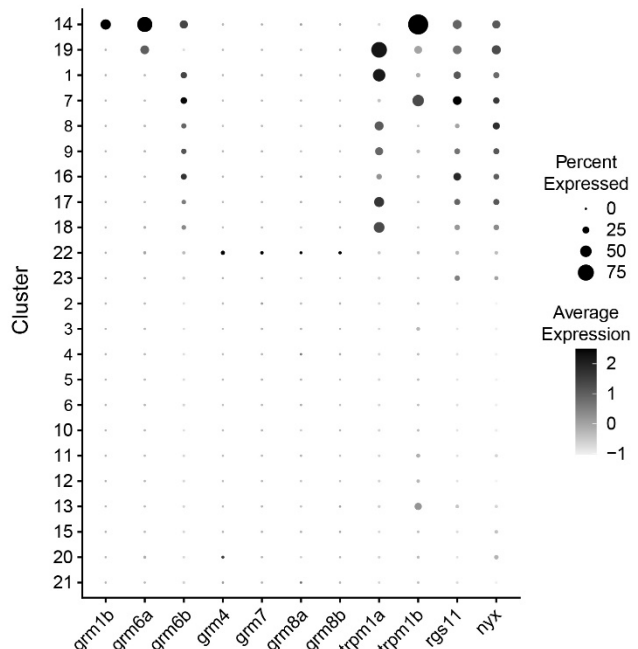


Figure S1. Expression patterns of the identified marker genes in BC clusters

a,b, The size of each circle depicts the percentage of cells in the cluster in which the marker was detected (≥ 1 UMI), and its grey scale depicts the scaled average expression level of cells within the cluster

c,e, Data for mouse is from Shekhar K, et al., 2016, Cell.

150 **RBC1 and RBC2 morphologies resemble mammalian RBCs**

151 We next determined the morphological similarities of RBC1 and RBC2 with mammalian RBCs. In
152 mammals, RBC axons arborize in the innermost layer of the IPL⁴¹. By screening our zebrafish
153 transgenic lines, we identified two lines, *Tg(vsx1:memCerulean)^{q19}* (*vsx1:memCer*) and
154 *Tg(vsx2:memCerulean)^{wst01}* (*vsx2:memCer*), that each label BCs with axon terminals in the
155 innermost layer of the IPL (Fig. 2). Fluorescent *in situ* hybridization for the identified gene markers,
156 *s100a10b* and *uts1*, which are selectively expressed by RBC1 and RBC2 (Fig. 1c), revealed that
157 *vsx1:memCer* and *vsx2:memCer* label RBC1 and RBC2, respectively (Fig. 2a,b). We also
158 observed that dendritic arbors of both RBC1 and RBC2 cover the retina in a non-overlapping
159 manner, an arrangement called 'tiling' that is considered a hallmark of a BC type (Fig. 2e,f)⁴².
160 Therefore, both RBC1 and RBC2 represent single bipolar types that transcriptionally and
161 morphologically resemble mammalian RBCs.

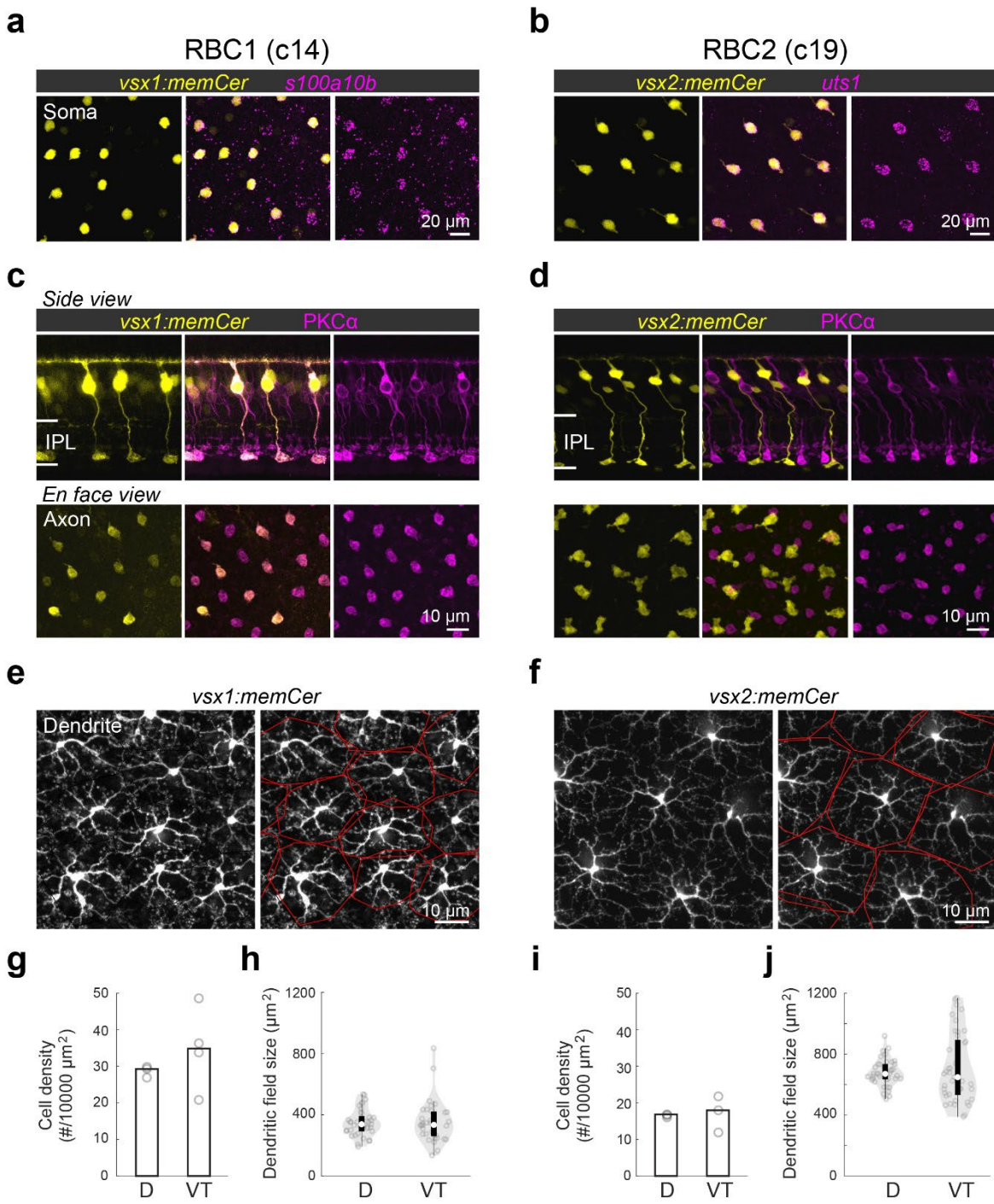
162 We observed slight variations in morphology and molecular expression between RBC1 and RBC2.
163 The axon terminal of RBC1 is relatively spherical, similar to mammalian RBCs, in contrast to the
164 'flat-footed' axonal ending of RBC2 (Fig. 2c,d). RBC1 were immunoreactive for PKC α (Fig. 2c),
165 whereas RBC2 were not (Fig. 2d), consistent with the difference in their *prkca* expression (Fig.
166 1d). In addition, their abundance differed: RBC1s were more densely packed than RBC2s
167 ($p=0.0052$, Mann-Whitney two-tailed U test) (Fig. 2g,i). This difference in the densities is unlikely
168 due to regional variations as both RBCs are present in the dorsal and ventral-temporal retina at
169 similar densities (Fig. 2g,i and Fig. S2). The dendritic field sizes of the two RBC types were
170 inversely related to their cell density, consistent with their tiling arrangement (Fig. 2g-j).

171

172

173

Figure 2



174 **Figure 2. Transgenic labeling of cluster 14 and 19 revealed morphological features of these**

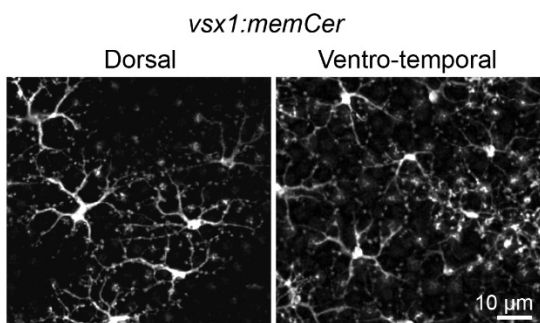
175 **BCs**

176 **a,b, En face view of retinal flat mount at the inner nucleus layer level. Cerulean fluorescent**
177 **expression (colored yellow) transgenic lines, Tg(*vsx1:memCerulean*)^{q19} (*vsx1:memCer*) in a and**

178 *Tg(vsx2:memCerulean)^{wst01}* (*vsx2:memCer*) in **b**. *vsx1:memCer* and *vsx2:memCer* BCs are
179 positive for cluster specific genes, *s100a10b* and *uts1*, respectively, which are detected using *in*
180 *situ* hybridization chain reaction⁴³. **c,d**, Side views of the labeled cells and the distribution patterns
181 of their axon terminals in *en face* views of retinal flat mounts for RBC1 (**c**) and RBC2 (**d**) BCs.
182 Immunolabeling for PKC α is in magenta. IPL: inner plexiform layer. Note that not all PKC-
183 immunoreactive cells are apparent in this image of the *vsx1:memCer* line, due to the incomplete
184 labeling of this line. **e,f**, Dendritic tiling of RBC1 (**e**) and RBC2 (**f**) in *en face* view of retinal flat
185 mounts at the outer plexiform layer level. Dendritic territories are marked by the red boundaries.
186 **g-j**, Mean cell densities of RBC1 (**g**, $n=3$ and 4 for D and VT, respectively) and RBC2 (**h**, $n=3$ for
187 both D and VT) BCs in different regions of the retina. Box and violin plots of dendritic field sizes
188 of RBC1 (**h**, $n=37$ and 33 or D and VT, respectively) and RBC2 (**j**, $n=40$ and 41 or D and VT,
189 respectively) BCs. White filled circles are medians. Grey circles indicate individual cells. D: dorsal,
190 VT: ventrotemporal.

Figure S2

a



b

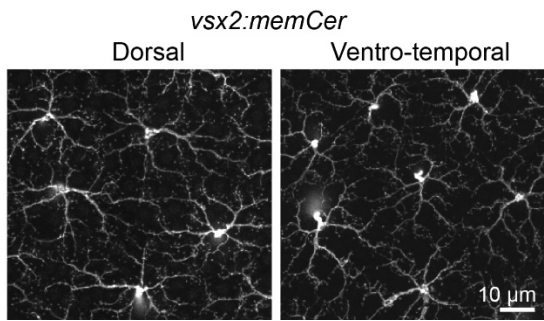


Figure S2. Dendritic tiling of RBC1 and RBC2

BCs across the retina

Confocal images of retinal flat mount at outer plexiform layer level from *Tg(vsx1:memCerulean)^{q19}* (*vsx1:memCer*) and *Tg(vsx2:memCerulean)^{wst01}* (*vsx2:memCer*). Note that the *vsx1:memCer* line occasionally labels OFF BCs. These BCs were distinguished by tracing the cells to the axon terminals in the confocal image volumes.

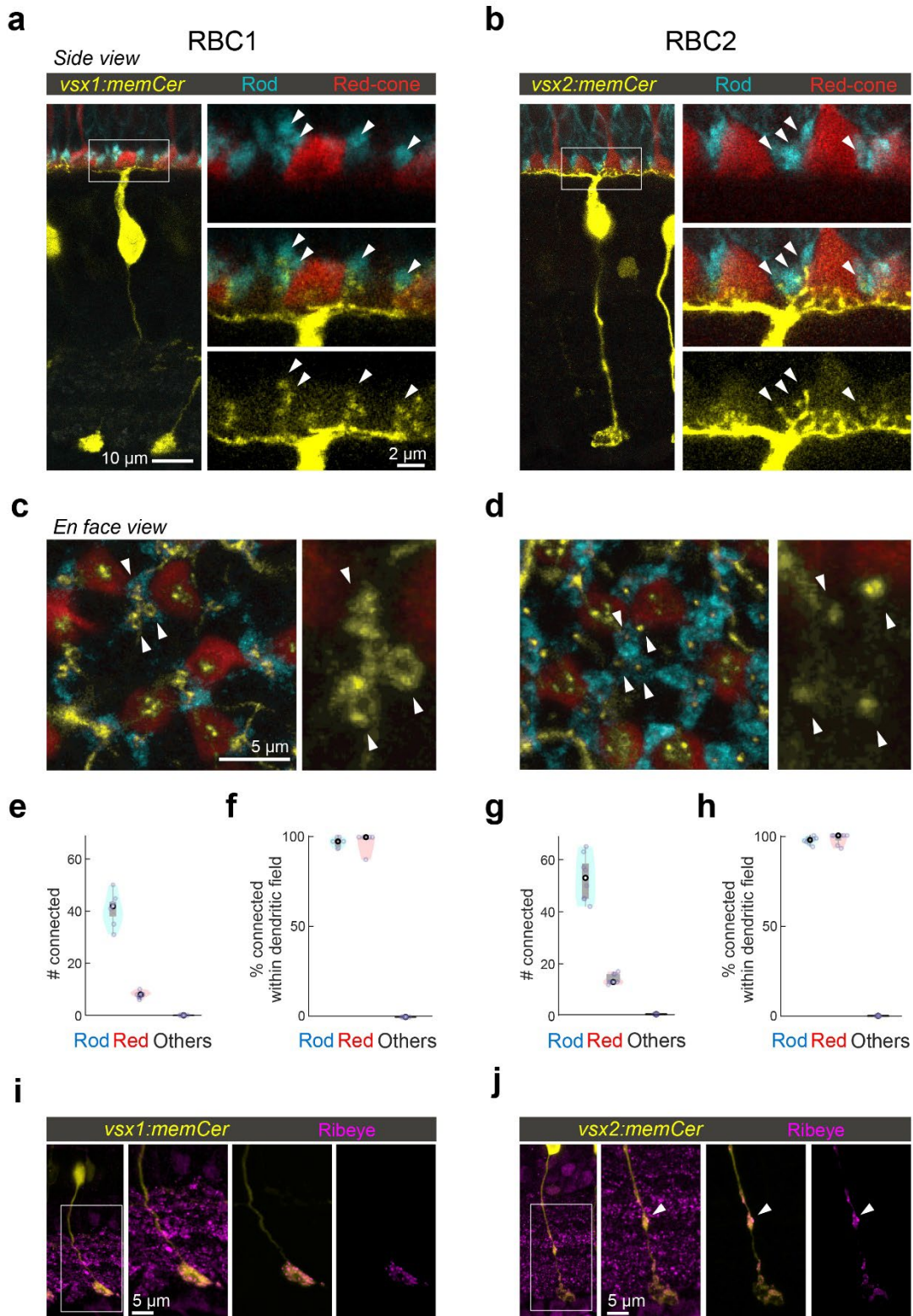
202 **Both RBC1 and RBC2 connect with all rods and red-cones in their dendritic territory**

203 If RBC1 and RBC2 are authentic RBCs, they should synapse preferentially with rods. Using 4C12
204 antibodies to label rods, we found that the majority of the dendritic tips of both RBC types (RBC1:
205 84±3.9%, RBC2: 78±2.9%) contacted with rod spherules (Fig. 3a-d). We also found that some
206 dendritic tips were not associated with rods (Fig. 3a-d). Using transgenic lines to label specific
207 cone types, we identified that dendritic tips of both BC types contacted red-cones (or long-
208 wavelength sensitive cones), labeled in the *Tg(trb2:tdtomato)*^{q22} line (Fig. 3a-e,g). Furthermore,
209 both types connected with nearly all rods and red cones within their dendritic fields (Fig. 3f,h). We
210 did not observe any dendritic tips that were not associated with either rods or red cones (Fig.
211 3e,g), indicating that they receive few if any inputs from the other cone types, which include green,
212 blue, and violet cones^{44,45}. Therefore, both RBC1 and 2 receive predominant rod input and share
213 specificity for red cones among cones (Fig. 3e,g).

214 Interestingly, the dendritic tips of RBC1 and RBC2 terminating in rod spherules differed in
215 structure (Fig. 3c,d). Specifically, the dendrites of RBC1 invaginating rod spherules appeared to
216 form a horseshoe or ‘doughnut’ ending, whereas those of RBC2 ended in a simpler arrangement
217 (Fig. 3c,d). The larger surface area of RBC1’s dendritic tips at rod terminals may increase the
218 sensitivity to rod inputs in this BC type compared to RBC2. We also observed differences in the
219 distal axonal boutons of RBC1 and RBC2 (Fig. 3i,j). While axons of both types terminate close to
220 the ganglion cells in the IPL, RBC2 axons have a bouton in the OFF layer of the IPL, next to the
221 boundary with the ON layer (Fig. 3j). These distal boutons are likely pre-synaptic sites as they
222 contain the pre-synaptic protein, Ribeye (Fig. 3j). These differences in the dendritic tip and axon
223 bouton shapes between RBC1 and RBC2 suggest that, while both BCs receive input from the
224 same combination of photoreceptor types, they may serve distinct visual functions.

225

Figure 3



227 **Figure 3. RBC1 and RBC2 connect to rods and red cones but differ in dendritic and axonal**
228 **synaptic arrangements**

229 **a,b**, Dendritic tips invaginating the rod and red cone axon terminals, visualized in retinal slices
230 from (a) $Tg(vsx1:memCerulean:trb2:tdtomato)^{q19,q22}$ and (b)
231 $Tg(vsx2:memCerulean:trb2:tdtomato)^{wst01,q22}$ adult zebrafish. Rods were immunolabeled using
232 4C12 antibody. **c,d**, Doughnut and simple dendritic tip structures at rod terminals (arrow heads)
233 in RBC1 and RBC2, respectively. **e-h**, Box and violin plots of RBC1 (**e,f**, $n=7$) and RBC2 (**g,h**,
234 $n=8$) connectivity with photoreceptors. **i,j**, Distribution of ribbon synapses in the RBC1 (**i**) and 2
235 (**j**) axons. Ribbons were immunolabeled by anti-ribeye antibody. Ribeye signals outside the axons
236 were digitally masked out in the right two images. RBC2 axon harbors a ribbon containing distal
237 bouton in the OFF layer (arrow head).

238

239 **RBC1 receives rod inputs via mGluR6 receptors**

240 We next asked whether zebrafish RBCs receive functional rod input via the metabotropic
241 glutamate receptor mGluR6 as seen in mammalian RBCs. We first investigated the expression of
242 mGluR6 in RBC1 and RBC2 dendritic tips at rod spherules. Super-resolution imaging of mGluR6
243 immunolabeling in *vsx1:memCerulean* and *vsx2:memCerulean* retinas showed that the dendritic
244 tips of RBC1, but not RBC2, robustly overlapped with mGluR6 immunoreactivity at contacts with
245 rod spherules (Fig. 4a,b). These findings are consistent with the transcriptional profiles, which
246 showed that RBC1 expresses higher mRNA levels of *grm6a* and *grm6b*, which encodes mGluR6,
247 than RBC2 (Fig. S1).

248 We then used electrophysiological recordings to ask whether mGluR6 mediates rod input to the
249 zebrafish RBCs. We prepared retinal wholemounts that preserve synaptic connections in the
250 outer retina, and performed whole-cell patch-clamp recordings on the axon terminals of RBC1

251 and RBC2 (Fig. 4c). Both RBC1 ($n = 10$) and RBC2 cells ($n = 3$) exhibited ON responses to a
252 cone-activating flash (red LED), confirming the successful patch-clamp recordings of light
253 responses in these BCs and demonstrating that both cell types are ON cells (Fig. 4d), consistent
254 with the position of their axonal arbors (Fig. 2c,d).

255 Although measuring rod-mediated responses from RBC2 was infeasible for technical reasons
256 (see Methods), we were successful in recording rod responses from RBC1. We were therefore
257 able to ask whether these responses were mediated by mGluR6. We presented rod-isolating dim
258 blue flashes (10 ms) before and after introducing the mGluR6 receptor agonist 6-(2-
259 aminopropyl)benzofuran (APB) to the perfusion solution. To isolate excitatory inputs to the cell,
260 all recordings were performed near the reversal potential for chloride-mediated conductances (~-
261 60 mV) and in the presence of inhibitory receptor blockers, gabazine, strychnine, and TPMPA
262 ((1,2,5,6-Tetrahydropyridin-4-yl)methylphosphinic acid). Our results showed that nearly all rod
263 inputs were blocked in the presence of APB, indicating that, like mammalian RBCs, mGluR6
264 mediates rod input to RBC1 (Fig. 4e).

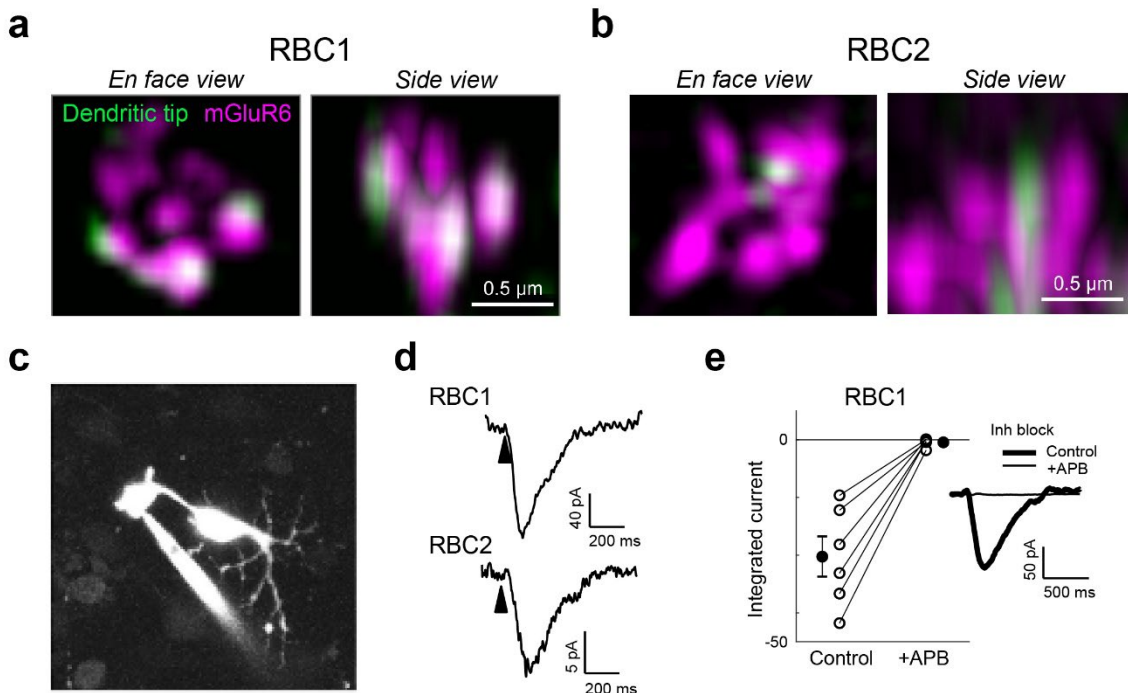
265

266 **Both RBCs primarily synapse onto amacrine cells**

267 To determine the synaptic targets of RBC1 and RBC2, we reconstructed their connectomes using
268 serial block face scanning electron microscopy (SBFSEM). In the reconstructions, we observed
269 an array of large BC axon terminals in the innermost layer of the IPL, which are characteristics of
270 RBC1 and RBC2 axons (Fig. S3a,b). To confirm that these large axon terminals belong to RBC1
271 and RBC2, we reconstructed dendrites of some of these BCs (Fig. 5a). Consistent with our
272 observations in light microscopic experiments (Fig. 3a-d), the large axon BCs predominantly
273 connect with rods.

274

Figure 4

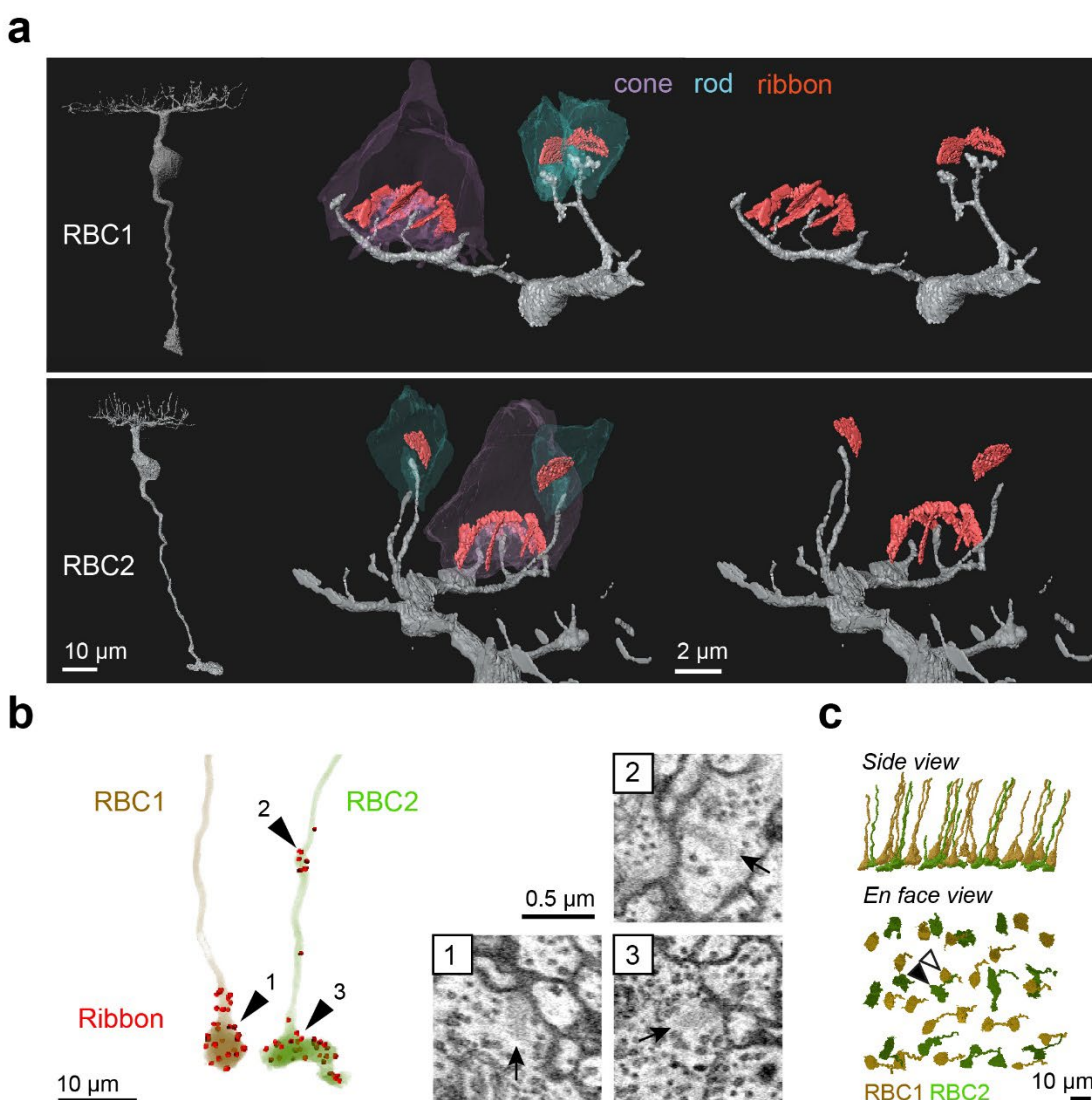


275 **Figure 4. Rod input to RBC1 is mediated by mGluR6 receptors.**

276 **a,b**, Confocal microscopy images of mGluR6 immunolabeling at rod terminals. **c,d**, Colocalization
277 of mGluR6 and RBC1 (**c**) and RBC2 (**d**) dendritic tips at rod terminals visualized by structured
278 illumination microscopy. **e**, Whole-cell patch clamping of a RBC1 axon terminal, visualized by dye-
279 filling Alexa Fluor 594). **f**, Voltage responses of RBC1 and RBC2 after a cone activating light flash
280 (arrow heads). **g**, Population data of RBC1 responses to rod activating light flashes with and
281 without the group III metabotropic glutamate receptor agonist, APB (6-(2-
282 aminopropyl)benzofuran). Filled circles: mean; error bars, S.D.; open circles, individual cells.
283 Traces on the right are an example of the cell's light evoked response before and during APB
284 bath application. Inhibitory neurotransmitter receptors were blocked (inh lock) by a bath
285 application of gabazine, strychnine, and TPMPA ((1,2,5,6-Tetrahydropyridin-4-
286 yl)methylphosphinic acid).

287 We then reconstructed all the large axons in the SBFSEM image volume. To distinguish RBC2
288 from RBC1, we used the ribbon containing axonal distal bouton in the OFF layer as a proxy for
289 RBC2 (Fig. 3i,j and Fig. 5b). These reconstructions revealed the regular mosaic arrangements of
290 both presumed RBC1 and RBC2 (Fig. 5c), indicating that we identified most, if not all, RBC1 and
291 RBC2 in the EM volume. Using this criterion, we also verified that dendritic tips of RBC1 are
292 doughnut shaped whereas those of RBC2 ended in a simple tip within the rod spherule, consistent
293 with our light microscopy data (Fig. 3c,d, 5a).

Figure 5



294 **Figure 5. Identification of RBC1 and RBC2 in a SBFSEM volume.**

295 **a**, Reconstructions of a RBC1 and a RBC2, and zoomed-in images of their dendritic tips at rod
296 and cone terminals. Ribbons in the rod and cones are painted red. **b**, Ribbon synapse distributions
297 in a RBC1 and a RBC2. The locations of ribbon synapses are marked in red. Arrow heads indicate
298 the locations of example ribbon synapses (arrows) shown in the insets. **c**, Reconstruction of all
299 RBC1s and RBC2s in the EM volume. Postsynaptic neurons of a centrally located RBC1 (open
300 arrow head) and RBC2 (closed arrow head) were reconstructed in Fig. 6, 7, and S4-8.

301

302 We then focused on one RBC1 and one RBC2 in the central area of the volume and traced all of
303 their post-synaptic neuronal processes (Fig. S3c,d). Amacrine cells (ACs), unlike reginal ganglion
304 cells (RGCs), make output synapses within the retina. Hence, we identified the neuronal class
305 (e.g. AC or RGC) for the majority (28/32) of the RBC1 postsynaptic processes and over the half
306 (18/31) of the RBC2 postsynaptic processes based on the presence or absence of presynaptic
307 structures. We found that both RBC1 and RBC2 predominantly synapse onto ACs (Fig. 6a,f). The
308 majority of the postsynaptic processes received 4 or fewer ribbon synapses from one RBC1 or
309 RBC2, with an exception of one process, which received 14 inputs from one RBC1 (Fig. 6b,g).

Figure S3

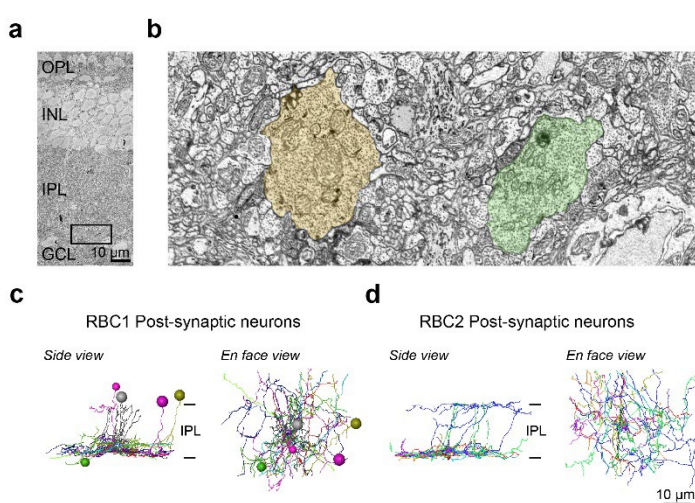


Figure S3. Identification of RBC1 and RBC2 postsynaptic neurons in SBFSEM volume

a, A partial image of an example SEM image of an adult zebrafish retina. OPL (outer plexiform layer), INL (inner nuclear layer), IPL (inner plexiform layer), GCL (ganglion cell

318 *layer). b, Magnified image of the region within the black box in a at the bottom layer of the IPL.*
319 *Characteristic large bipolar cell axons are painted in light yellow and green. c,d, Traces of*
320 *neuronal processes and the location of somas of cells that are post-synaptic to RBC1 and RBC2*
321 *cells. Individual cells were color coded. IPL: inner plexiform layer.*

322

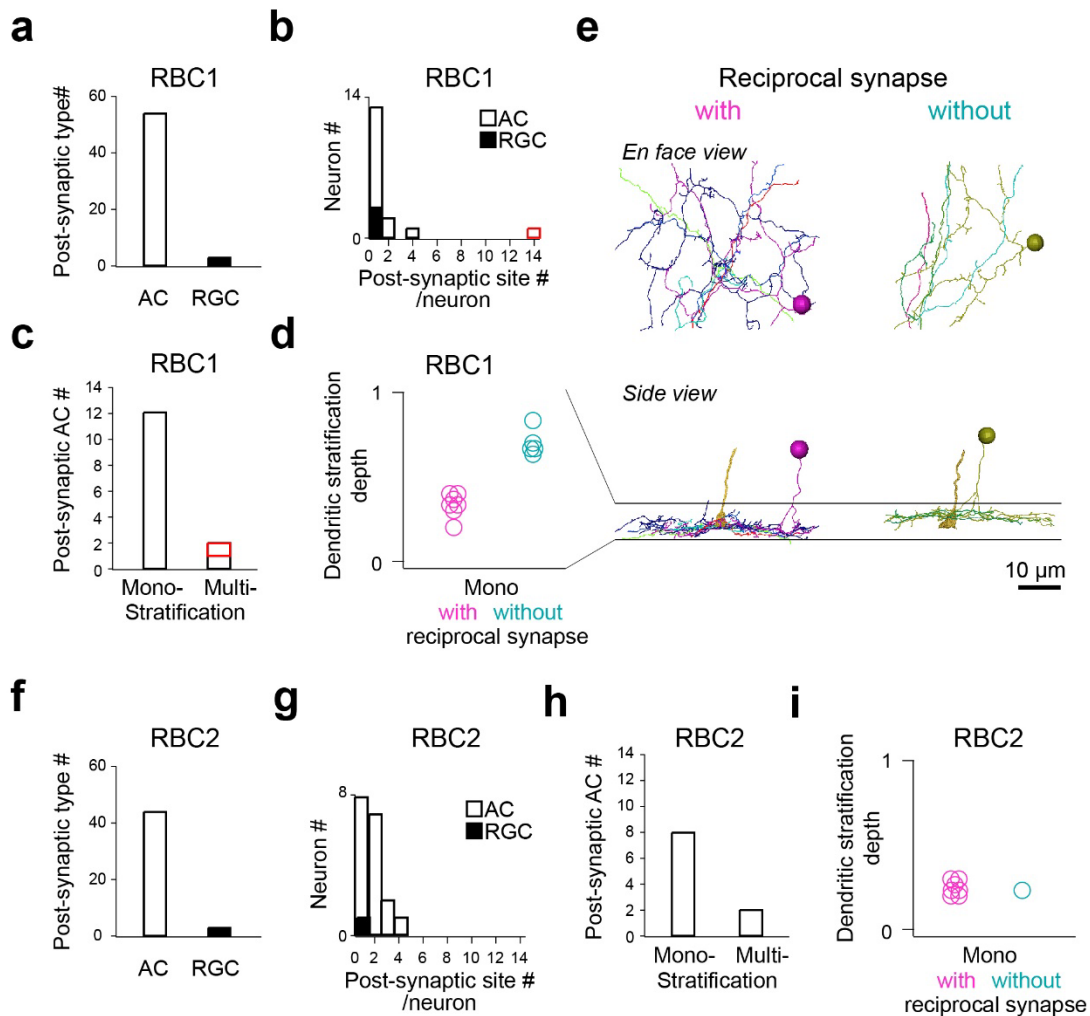
323 We further morphologically classified the postsynaptic ACs that we traced, comprising 14 cells for
324 RBC1 (Fig. S4-6) and 10 cells for RBC2 (Fig. S7,8), respectively. Most ACs extended their
325 dendrites within a single sublamina in the IPL (Fig. 6c,h). Among these mono-stratifying ACs for
326 RBC1, we identified two groups based on their dendritic stratification depth within the IPL (Fig.
327 6d,e). These two groups of ACs differed in their synaptic arrangement. ACs stratifying in the lower
328 layer formed reciprocal synapses (RS) – a synaptic arrangement that includes both input and
329 output synapses with a BC axon - with RBC1, whereas ACs stratifying in the upper layer did not
330 (Fig. 6d,e, Fig. S4,5). For RBC2, all but one AC (1/8) formed local reciprocal synapses (Fig. 6i,
331 Fig. S7,8). In addition, RBC1 formed an exceptionally high number of ribbon connections with one
332 bi-stratifying AC (marked in red in Fig. 6b,c, morphology in Fig. 7d,e and Fig. S6). In contrast,
333 RBC2 does not have a post-synaptic partner with extensive synapses.

334 Taken together, these results demonstrated that RBC1 allocated the majority (91%) of synaptic
335 outputs to 3 types of AC: 14% to non-RS ACs, 37% to RS ACs, and 40% to one bi-stratifying ACs.
336 In contrast, the RBC2 we reconstructed synapsed primarily onto a mono-stratifying AC type (68%).
337 Among 24 ACs that we traced throughout the volume, only 5 were shared between RBC1 and
338 RBC2 (Fig. S4-8). Therefore, the downstream circuits of these BC types are largely separate at
339 least at the AC level.

340

341

Figure 6



342

343 **Figure 6. Identification RBC1 and RBC2 post-synaptic neuron types**

344 **a-d**, Quantification of morphological parameters of neurons postsynaptic to one of the RBC1s in
 345 the EM volume (marked by an open arrow head in Fig. 5c). One postsynaptic neuron contained
 346 an exceptionally higher number of synapses (14) with the RBC1 (marked in red in **b** and **c**).
 347 Dendritic stratification is normalized to 0 and 1 at the lower and upper ends of the RBC1 axon
 348 terminals, respectively in **d**. **e**, Mono-stratifying ACs with (red) or without (blue) reciprocal
 349 synapses with RBC1s in the volume. The axon of the presynaptic RBC1 is also shown in the side

350 view. Individual cells were color coded. **f-i**, Quantification of morphological parameters for
351 neurons postsynaptic to one of the RBC2s in the EM volume (marked by a closed arrow head in
352 Fig. 5c). AC: amacrine cells, RGC: retinal ganglion cells.

353

354 **The wiring diagram of RBC1 resembles that of the mammalian primary RBC pathway**

355 Finally, we compared the targets of RBC1 and RBC2 with those known to comprise the primary
356 rod pathway in the mammalian retina. Mammalian RBCs synapse onto a mono-stratified AC type
357 called A17 and a bi-stratified AC type called A2^{3,5-7}. A17 ACs are wide field ACs that synapse
358 exclusively with RBCs and form reciprocal synapses with them^{31,46}, whereas A2 ACs are narrow
359 field ACs that receive numerous (~40) synapses from RBCs but do not form reciprocal synapses
360 with them^{18,30}. Instead, A2 ACs form gap-junctions with ON CBCs through dendrites in the ON
361 layer and output synapses onto OFF CBCs through the bouton structures in the OFF layer called
362 lobular appendages³².

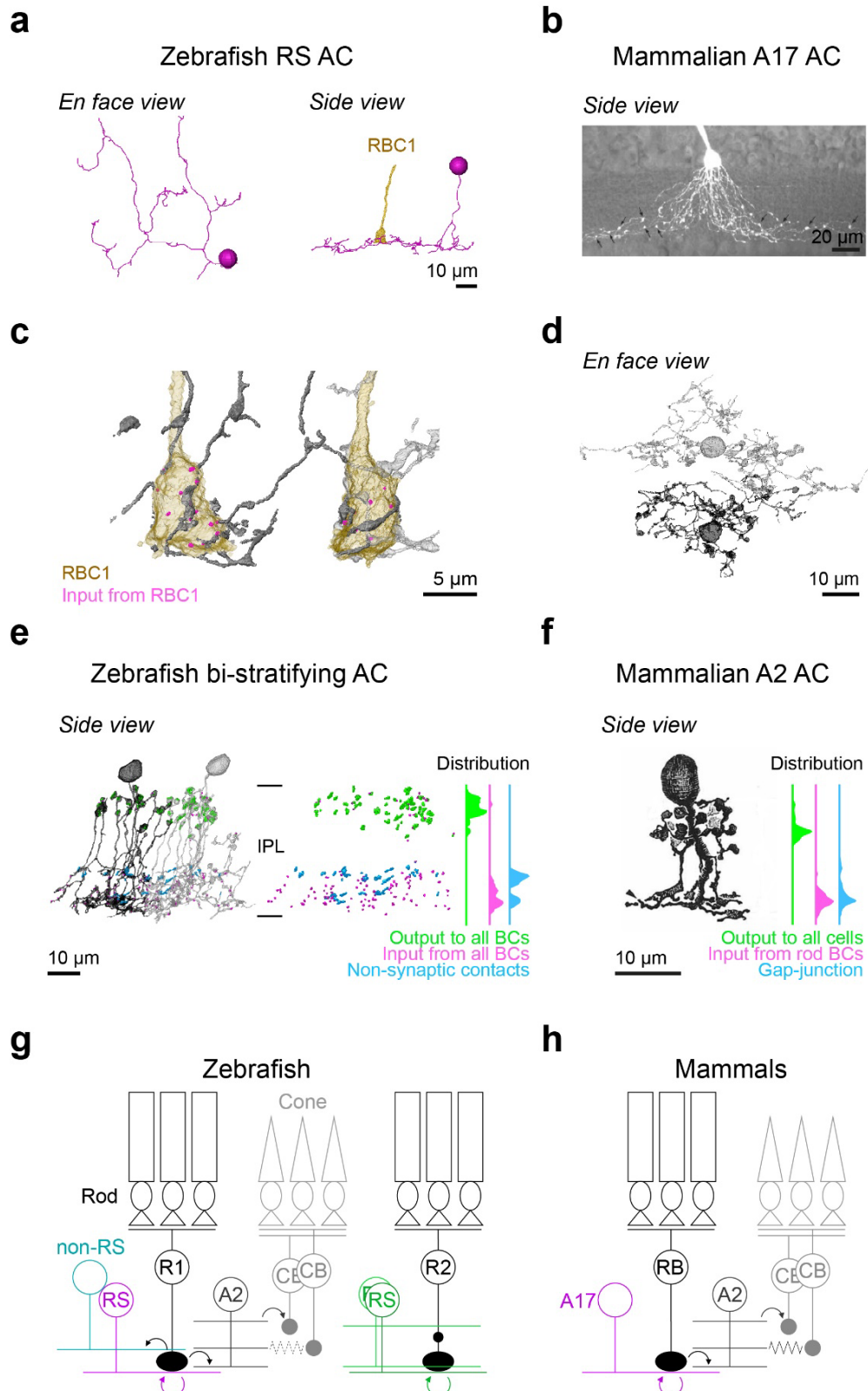
363 We found that zebrafish RBC1s synapse onto both wide field ACs with reciprocal synapses (the
364 RS ACs)(Fig. 6,7a), resembling mammalian A17s (Fig. 7b), and a narrow field bi-stratifying ACs
365 with extensive synaptic connections, resembling mammalian A2s (Fig. 6,7c-f). By marking
366 synaptic sites of RS ACs throughout their dendrites, we found that RS ACs are dedicated to the
367 RBC1 pathway; synapsing predominantly (both input and output) with RBC1 and to a lesser extent
368 with RBC2 (Fig. S4), with no synapses with other BC types (n=7 cells). This synaptic specificity
369 and the reciprocal synapse arrangement in RS ACs mirror those of mammalian A17 ACs³¹.

370

371

372

Figure 7



374 **Figure 7. Circuit diagram of RBC1 is similar to mammalian RBC pathway**

375 **a**, An example monostratified amacrine cell (RS AC) classified in Fig. 6e that formed of reciprocal
376 synapse with RBC1. **b**, A mouse A17 amacrine cells (taken from⁴⁷) (**b**). **c,d**, A2-like ACs that are
377 postsynaptic to two neighboring RBC1s. **e,f**, Locations and distributions of synaptic sites and
378 non-synaptic contacts with BCs in zebrafish bi-stratifying AC (**e**) and in rabbit A2 ACs (taken from
379 ³²) (**f**). Note that synapses or non-synaptic contacts with AC and RGC are not included in (**e**), and
380 inputs from CBC are not included in (**f**). **g,h**, Schematic diagrams of zebrafish (**g**) and mammalian
381 (**h**) RBC pathways. Mouse A17 and rabbit A2 images are from⁴⁷ and³², respectively, used with
382 permissions. Data for the distributions of synaptic sites within mammalian A2 ACs across the
383 inner plexiform layer (IPL) are taken from⁴⁸.

384

385 Next, we examined the synaptic arrangements of RBC1 with the A2-like ACs. First, we confirmed
386 that this type of AC is common to other RBC1s. By tracing the postsynaptic processes of
387 neighboring RBC1, we found another A2-like AC, which received a high number of ribbon inputs
388 from the neighboring RBC1 (Fig. 7c,d). We marked the locations of synapses with all BCs for
389 those two ACs (Fig. 7e). Gap-junctions are too small to be resolved in our SBFSEM images, but
390 as a proxy, we marked non-synaptic contacts (Fig. 7e). These revealed a striking similarity in the
391 distribution patterns of synapses and (potential) gap-junction sites across the IPL layers between
392 this AC type in zebrafish and mammalian A2 ACs (Fig. 7e,f), including the bouton structures in
393 the OFF layer that contain large presynaptic sites^{48–50}. Taken together, we conclude that the circuit
394 diagram among mammalian RBC, A2, and A17 ACs are conserved in the zebrafish RBC1
395 pathway (Fig. 7g,h).

396 In contrast to the targets of RBC1, RBC2 formed synapses exclusively with wide-field ACs (Fig.
397 S7,8) and lack a synaptic partner with extensive synapses. Thus, RBC2 participates in a circuit
398 that differs from that of mammalian RBCs.

399

400 **DISCUSSION**

401 By combining scRNA-seq, electrophysiology, and light and electron microscopy circuit
402 reconstructions, we demonstrated that RBC1 shares many features with the mammalian primary
403 rod pathway (Fig. 7g,h), implying that the conserved rod pathway is evolutionarily ancient.

404 **The number of BC types**

405 In this study, we found 23 molecular types in adult zebrafish BCs. However, a previous
406 morphological characterization of zebrafish BCs, based on their dendritic connectivity with
407 photoreceptors and axon stratifications, identified 32 anatomical types⁵¹. The discrepancy in the
408 number of BC types between morphological and transcriptional characterizations may arise from
409 the regional specializations that have been documented in the larval zebrafish retina⁵²⁻⁵⁵. In any
410 event, it is clear that the adult zebrafish retina contains at least 23 BC types.

411 This number of molecular types of bipolar cells (BCs) in zebrafish, as identified in this study, is
412 higher than that found in mammals investigated to date (14-15 across mammals)^{26,27,29,56}, but
413 similar to that found in chick retina (22 molecular and 15 morphological BC types)^{57,58}. The higher
414 number of BC types in zebrafish and chicken is not surprising, given that these species have
415 higher numbers of photoreceptor types: 5 in zebrafish and 7 in chicks, compared to ≥ 3 in
416 mammals^{59,60}. We demonstrate here one source of the increase: a single type of BC carries most
417 of the input from rods in mammals, whereas zebrafish has two RBC types.

418 **The number of RBC types**

419 Previous morphological characterization of zebrafish BCs found only one BC type that connects
420 rods and red cones. Axons of these BCs terminate in the innermost layer of the IPL⁵¹. We
421 speculate that this type actually includes both RBC1 and RBC2, which were combined owing to
422 their striking morphological similarity (Fig. 2,3). Consistent with this hypothesis, studies in goldfish
423 have reported two morphologically distinct “mixed” BC types that receive dominant inputs from
424 rods²². They have large axon terminals at the bottom of the IPL, but the axon of one mixed BC
425 type contains a smaller axonal distal bouton in the OFF layer, similar to RBC2⁶¹. Immunostaining
426 for PKC only labels mixed BCs without an axonal distal bouton, similar to RBC1⁶². The presence
427 of these features in goldfish suggests that RBC1 and RBC2 are conserved among teleost fish.

428 Much less is known about RBCs in other non-mammalian vertebrate species. In salamander, one
429 type of mixed ON BCs exhibit sensitivity close to that of rods^{14,63}. They terminate their axons at
430 the bottom of the IPL, similar to teleosts and mammals, but it is unknown whether they express
431 the RBC marker PKC. Furthermore, the anatomical connections of BCs with rods are not yet
432 comprehensively studied in salamander. In birds, PKC labels some ON layer stratifying BC types
433 strongly^{64,65}. Single-cell RNA-sequencing of chick BCs revealed a BC type that is
434 transcriptomically similar to the mammalian RBCs⁵⁸. However, the physiological properties and
435 connections of these BCs are unknown. Moreover, a connectomic survey of chick BC types failed
436 to identify BC cells that connect with all rods in their dendritic field⁵⁷. Unlike the species mentioned
437 above, the presumed rod bipolar cells, which have light sensitivity close to that of rods, in sea
438 lamprey are OFF type⁶⁶. However, their connectivity with rods is unknown. Thus, it remains
439 unclear whether RBC2 orthologs are present in species other than zebrafish.

440 In mammals, morphological, molecular, and functional studies have identified only a single RBC
441 type^{23,26,27,67}. Therefore, we speculate that either RBC2 evolved after the divergence between
442 teleost fish and mammals, or mammals lost this pathway.

443 **Roles of cone inputs in RBCs**

444 Cone inputs onto rod-dominant mixed BCs have been proposed to broaden the dynamic range of
445 light intensities to which they can respond⁶⁸. Consistent with this idea, we found that both RBC1
446 and RBC2 are selective for red cones, which, with their broad spectral sensitivity, are suited for
447 encoding achromatic luminance information⁶⁹. Because rods evolved from cones¹, we speculate
448 that RBCs may have emerged from red-cone specific CBCs. The red cone selectivity is also
449 conserved in at least one of the mixed rod dominant BC types in goldfish⁷⁰. Although cone
450 selectivity is unknown in Salamander rod-driven mixed BCs, their spectral sensitivity curve is
451 broader at longer wavelengths than that of rods, indicating that they may connect to red cones¹⁴.

452 Electrophysiological recording from rod-driven BCs in *Giant Danio*, a teleost fish species, showed
453 that rod and cone inputs onto rod-dominant BCs are mediated by different mechanisms: rod inputs
454 through mGluR6, whereas cone inputs through both mGluR6 and EAAT (excitatory amino acid
455 transporter)⁶⁸. In this BC type, mGluR6 and EAAT-mediated inputs suppress each other, likely to
456 allow this cell to respond to both rod and cone dynamic ranges⁶⁸. Electrophysiological recordings
457 in zebrafish found that some of ON BCs responded to glutamate via both mGluR6 and a
458 glutamate-gated chloride conductance increase mechanism, which is likely through EAATs⁷¹.
459 However, the nature of EAAT contributions for cone responses in RBC1 and RBC2 is unknown.

460 While the study in *Giant Danio* suggest that mixed inputs expand the dynamic range of rod-
461 dominant BCs, electrophysiological recordings in goldfish and salamander have found that the
462 dynamic range of rod dominant BCs is similar to that of rods and that cone contributions to the
463 light response are small^{14,72}. Therefore, the roles of red-cone inputs to RBCs remain to be
464 determined.

465 **Unifying mixed BCs and RBCs**

466 In mammals, it was initially thought that RBCs exclusively synapse with rods⁷³. However, several
467 recent studies have demonstrated convincingly that RBCs also receive synapses from cones, at

468 least in mice, rabbits, and primates^{8,73-75}. Indeed, mouse RBCs contact the majority of M-cones
469 (~80%), which are analog of zebrafish red-cone, in their dendritic territories⁸. RBCs were likely
470 thought to be exclusive to rods because of the high ratio of rods to cones in the outer nuclear
471 layer in mice and rabbits^{76,77}. As a consequence, only a few cones, generally three or fewer,
472 synapse on a mouse RBC, compared to inputs from ~35 rods^{8,75}.

473 The rod-driven BCs in non-mammals are classically called “mixed” BCs because they connect
474 with both rods and cones. However, as argued above, this mixed connectivity is conserved in the
475 mammalian RBCs. Moreover, the dendritic specificity and connectivity of RBCs are conserved in
476 mice and zebrafish. In both species, RBCs connect with all rods and the majority of red-cones (or
477 M-cones) in their dendritic fields (Fig. 3f,h). Therefore, converging rod and red-cone inputs is likely
478 a conserved feature of RBCs in all vertebrates. This leads us to propose that the non-mammalian
479 mixed BCs and the mammalian RBCs represent a single class of neurons, RBCs. Finally, taken
480 together with the striking similarity in the downstream circuitry of RBCs between zebrafish and
481 mammals, we conclude that zebrafish RBC1 is transcriptomically, anatomically, and functionally
482 equivalent of mammalian RBC and that they share the same evolutionary origin.

483

484 **ACKNOWLEDGEMENTS**

485 We thank the Vision Core at the University of Washington for processing zebrafish retina samples
486 and acquiring serial images for SBF-SEM. We thank Rachael N. Swanstrom for helping with cell
487 tracing of the EM volume. Funding was provided by the MCSA fellowship (“ColourFish” 748716)
488 from the EU Horizon 2020 to TY, the NIH EY14358 to ROW, U01MH105960 and R01 EY022073
489 to JRS, EY01730 (Vision Core grant, P.I. M. Neitz) Developmental Biology Training Grant
490 HD07183 to FDD, The Wellcome Trust 220277/Z20/Z to TB, European Research Council ERC-
491 StG 677687 to TB, UKRI BBSRC, BB/R014817/1 and BB/W013509/1 to TB, Leverhulme Trust

492 PLP-2017-005; RPG-2021-026 to TB, NIH grant R00EY028625 to KS, Hellmann Foundation
493 Fellowship to KS, travel grant from Graduate School in Systemic Neuroscience to YK, and Max
494 Planck Society to YK and HB.

495

496 **AUTHOR CONTRIBUTIONS**

497 TY, ROW, AMH, PM, JH, and YK designed the study, with input from KS, JRS, HB, and TB. YK
498 performed single-cell RNA-seq, under the supervision of HB and JRS with guidance from KS. JH
499 processed and analyzed the data with guidance from KS; TY and SCS generated new plasmids;
500 TY and FDD generated novel lines; TY performed experiments, collected and analyzed the data
501 for light microscopy with help from OL; PM performed whole-cell patch recordings; FDD prepared
502 the sample for SBF-SEM; AMH, OL, and TY traced the EM images; TY analyzed the EM data;
503 TY wrote the manuscript with inputs from all authors.

504

505 **DECLARATION OF INTERESTS**

506 The authors declare no competing interests.

507

508

509

510

511

512

513

514 **MATERIALS AND METHODS**

515 **Animals**

516 All procedures were performed in accordance with the University of Washington Institutional
517 Animal Care and Use Committee guidelines, the Harvard University/Faculty of Arts & Sciences
518 Standing Committee on the Use of Animals in Research and Teaching (IACUC), and the UK
519 Animals (Scientific Procedures) act 1986 and approved by the animal welfare committee of the
520 University of Sussex. For all experiments, we used adult zebrafish (age 6-18 months) of either
521 sex that were kept at 28°C in a room with a normal 14/10 light cycles.

522 The following previously published transgenic lines were used: *Tg(vsx1:GFP)^{nns5}*⁷⁸,
523 *Tg(vsx1:memCerulean)^{q19}*⁷⁹, *Tg(trb2:tdtomato)^{q22}*⁸⁰. In the larva *Tg(vsx1:memCerulean)^{q19}* labels
524 a subpopulation of OFF layer stratifying BCs⁷⁹. In adults, while OFF stratifying BCs are still weakly
525 labeled, Cerulean is now strongly expressed in RBC1 (Fig. 2a,c). In addition,
526 *Tg(vsx2:memCerulean)^{wst01}* line was generated by injecting pBH-vsx2-memCerulean-pA plasmid
527 into single-cell stage eggs. Plasmid was diluted in 1x Danieu's solution to a concentration of 50
528 ng/ml. Plasmid solution was loaded into a pulled-glass micropipette, mounted to a
529 micromanipulator (Narishige), and pressure-injected via attachment to a Picospritzer II (Parker).
530 Injections were made at 10 psi for durations from 100 to 200 ms. Injected fish were raised and
531 out-crossed with wild-type fish to screen for founders. Positive progenies were raised to establish
532 transgenic lines.

533 **BC single cell RNA sequencing**

534 *BC purification and sequencing*

535 Adult zebrafish carrying the *Tg(vsx1:GFP)^{nns5}* transgene were used to isolate BCs for single-cell
536 RNA sequencing. Retinas were dissected and digested in papain solution containing 20U/ml
537 papain, 80U/ml DNasel, and 1.5mM L-cysteine in oxygenated (ox) Ames solution at 28°C for 45

538 minutes. The digestion was stopped by replacing the papain solution with a papain inhibitor
539 solution containing 15mg/ml ovomucoid and 15mg/ml BSA. The tissue was gently dissociated by
540 trituration using a flamed glass pipette and washed with ox. Ames containing 0.4% BSA. The
541 resulting cell suspension was filtered through a 30 μ m strainer and fluorescence-activated cell
542 sorting (FACS) was performed. Non-transgenic wild-type retinas were used to determine
543 background fluorescence levels and adjust sorting gates. Live bipolar cells were distinguished
544 using Calcein blue. Cells were washed, resuspended in PBS 0.04% BSA, and loaded onto the
545 microfluidic device within ~45 minutes after FACS enrichment. Droplet RNA sequencing
546 experiments were conducted on the 10X chromium platform according to the manufacturer's
547 instructions with no modifications. Up to sixteen retinas from up to eight fish per batch were
548 dissected and dissociated. Eight cDNA libraries were generated across four experiments with two
549 replicates each. The cDNA libraries were sequenced on an Illumina HiSeq 2500 to a depth of
550 ~30,000 reads per cell.

551 *Single cell transcriptomics data analysis*

552 We performed the initial preprocessing using the cellranger software suite (version 2.1.0, 10X
553 Genomics), following steps described previously in our study of Zebrafish RGCs⁸¹. The
554 sequencing reads were demultiplexed using “cellranger mkfastq” to obtain a separate set of
555 fastq.gz files for each of 8 samples, which were distributed across Y biological replicates. Reads
556 for each sample were aligned to the zebrafish reference transcriptome (ENSEMBL zv10, release
557 82) using “cellranger count” with default parameters to obtain a binary alignment file and a filtered
558 gene expression matrix (GEM) for each sample. To account for intronic reads, the binary
559 alignment files were processed using velocyto with default parameters⁸², producing a loom file
560 containing a GEM for exonic reads and a separate matrix for intronic reads. The matrices were
561 combined for each sample, resulting in a total gene expression matrix (GEM; genes x cells)
562 summarizing transcript counts. We used the Seurat R package (Stuart et al., 2019) to combine

563 the GEMs from different channels and analyzed them for each of the biological replicates, unless
564 otherwise stated, with default parameter values. Additionally, we evaluated the robustness of our
565 clustering results to variations in select parameters. The full details of our analyses are
566 documented in markdown scripts, which are available at
567 <https://github.com/shekharlab/ZebrafishBC>.

568 *Preprocessing and batch integration*

569 The combined GEM was filtered to remove genes expressed in fewer than 25 cells, and cells
570 expressing fewer than 50 genes resulting in 25,233 genes and 19,492 cells. Briefly, each cell was
571 normalized to a total library size of 10,000 and the normalized counts were log-transformed using
572 the function Seurat::NormalizeData. We used Seurat::FindVariableFeatures with option
573 selection.method = "vst" to identify the top 2000 highly variable genes (HVGs)⁸³ in each batch.
574 Next, we performed scRNA-seq integration. We used Seurat::FindIntegrationAnchors and
575 Seurat::IntegrateData, both with options "dims=1:40" to perform Canonical Correlation Analysis
576 (CCA)-based batch correction on the reduced expression matrix consisting of the HVGs. The
577 "integrated" expression values were combined across replicates, and used for dimensionality
578 reduction and clustering.

579 *Dimensionality Reduction, Clustering and Visualization*

580 To remove scale disparities between genes arising from differences in average expression levels,
581 the integrated expression values for each HVG were z-scored across the cells using
582 Seurat::ScaleData. Next, we performed Principal Component Analysis (PCA) on the scaled matrix,
583 and used Seurat::ElbowPlot to select principal components (PCs). Using the top 20 PCs, we built
584 a k-nearest neighbor graph using Seurat::FindNeighbors and identified transcriptionally distinct
585 clusters using Seurat::FindClusters, using a resolution parameter of 0.5.

586 Using the top 20 PCs, we also embedded the cells onto a 2D embedding using Uniform Manifold
587 Approximation (Becht et al., 2019) using the Seurat function RunUMAP.

588 *Identification of BCs and filtering contaminant classes*

589 BC clusters were identified based on expression of the pan-BC markers *vsx1*, and other cell
590 classes were filtered based on well known gene markers Examples of such genes include *rlbp1a*
591 and *apoeb* for Muller glia⁸⁴, *rbpms2b* for retinal ganglion cells⁸⁵, *gad1* and *gad2* for amacrine
592 cells⁸⁶, *pde6* for photoreceptors⁸⁷, and *cldn19* for endothelial cells⁸⁸. A total of 155 cells
593 corresponding to these cell classes were removed.

594 *Hierarchical clustering*

595 To identify transcriptional relationships between BC clusters, we used
596 Seurat::FindVariableFeatures to recalculate the top 2000 most variable genes. The average
597 expression values of genes in each cluster were used as input for hierarchical clustering,
598 performed using pvclust with parameters method.hclust = "complete" and method.dist =
599 "correlation". The resulting output was visualized as a dendrogram.

600 **Plasmid construction**

601 Plasmid pBH-vsx2-memCerulean-pA was made using the Gateway system (ThermoFisher,
602 12538120) with combinations of entry and destination plasmids as follows: pTol2CG2⁸⁹, p5E-vsx2,
603 pME-membrane-Cerulean, p3E-pA⁸⁹. Plasmid p5E-vsx2 was generated by inserting a
604 polymerase chain reaction (PCR)-amplified vsx2 promoter genomic fragment into p5E plasmid
605 using BP clonase (ThermoFisher, 11789013). PCR reaction was performed using primers: 5'-
606 GGGGACAACCTTGTATAGAAAAGTTGATGCTAACAACTTCAAACGACCAA-3' and 5'-
607 GGGGACTGCTTTTGACAAACTTGGCCTCTGAGACTATTCCCTTCTTG-3'.

608 **Immunostaining and light microscopy imaging**

609 Adult zebrafish were humanely euthanized in ice-chilled fish water. After decapitation, retinal
610 tissues were dissected from the enucleated whole eyes by removing cornea, lens, and epithelial
611 layer in 1x in phosphate-buffered saline (PBS). The tissue were immediately fixed in 4%
612 paraformaldehyde (Agar Scientific, AGR1026) in PBS for 20 min at room temperature (RT)
613 followed by three washes in PBS. For retinal slice preparation, the tissues were mounted in 2%
614 agarose in PBS and sliced at 100 or 200 μ m thickness using vibratome (TPI 1000). For rod
615 staining, the tissues were sliced horizontally, parallel to the outer plexiform layer (OPL), to
616 facilitate antibody penetration in the tissue while preserving bipolar cell dendrites in the OPL.
617 Sliced or the whole retinal samples were treated with PBS containing 0.2% Triton X-100 (Sigma-
618 Aldrich, X100) for at least 10 min and up to 1 day, followed by the addition of primary antibodies.
619 After 3 to 5 days of incubation at 4°C, samples were washed three times with PBS and 0.2%
620 Triton X-100 solution and treated with secondary antibodies. After 1 day of incubation, samples
621 were mounted in 1% agar in PBS on a coverslip, and subsequently, PBS was replaced with
622 mounting media (VECTASHIELD, H-1000) for imaging.

623 Primary antibodies were 4C12 antibody (mouse, 1:50; kindly provided by Jim Fadool⁹⁰ and anti-
624 mGluR6b antidoby (rabbit, 1:500; kindly provided by Stephan CF Neuhauss⁹¹). Secondary
625 antibodies were AlexaFluor594 anti-rabbit (donkey, 1:500; Jackson ImmunoResearch
626 Laboratories 711-586-152) and DyLight647 anti-mouse (donkey, 1:500; Jackson
627 ImmunoResearch Laboratories 715-606-150). Confocal image stacks were taken on a TCS SP8
628 (Leica) with a 63 \times oil immersion objective (HC PL APO CS2, Leica). Typical voxel size was 90
629 nm and 0.5 μ m in xy and z, respectively. Super-resolution images were taken on an OMX (General
630 Electric). Contrast, brightness, and pseudo-color were adjusted for display in Fiji [National
631 Institutes of Health (NIH)].

632 Image stacks were median filtered in Fiji. For some images, maximum-intensity projections were
633 generated in Amira (FEI). 3D image reconstructions were digitally sliced using the Amira slice
634 functions. All measurements were made in Fiji.

635 **Image Analysis**

636 *Quantitation of cell density*

637 We obtained the cell density of RBC1 and RBC2 by counting the axon terminals of these cells
638 within regions of interest from confocal image stacks of the dorsal and ventro-temporal retina.
639 RBC2 was counted from images of the *Tg(vsx2:memCerulean)^{wst01}* line. Because not all RBC1
640 labeled in the *Tg(vsx1:memCerulean)^{q19}* line express mCerulean, we quantified the density of
641 PKC labeled cells with axon terminals in the bottom layer of the IPL. Counts were obtained from
642 3-4 retinas from 3 animals of each line. For RBC1, axons were quantified within an area between
643 37,000 and 85,000 μm^2 , and for RBC2, the areas were between 11,000 -22,000 μm^2 .

644 *Dendritic field*

645 The dendritic field was defined by tracing the extent of a given cell's dendrites with the polygonal
646 select tool, and removing any concavity using FIJI (see Figure S2). The dendritic arbor area was
647 then obtained by calculating the area enclosed by the polygon. Because the dendritic tips of some
648 neighboring cells of the same type overlapped and could not be distinguished readily, one
649 investigator repeatedly traced (3 to 4 measurements for a single cell) the dendrite boundary, and
650 obtained the respective area for a given cell until at least three measurements were within $\pm 2.5\%$
651 of the average of all previous measurements for that cell. Confocal images from three fish were
652 used, with images of RBC1 and RBC2 cells acquired from the dorsal and ventral regions of the
653 retina: 10 to 17 cells per fish were measured for each location and cell type, resulting in a total of
654 33 to 41 cells measured for each location and cell type.

655 *Photoreceptor connectivity*

656 Dendritic contacts with photoreceptors were defined by the co-localization of dendritic tips
657 extending towards outer nucleus layer and photoreceptor terminals by scrolling through confocal
658 image stack in Fiji. The percentage contacted was computed by dividing the number of
659 photoreceptors contacted by a given BC by the number of photoreceptors within the dendritic field
660 of the BC.

661 **Electrophysiology**

662 Fish (3-6 months old) used in physiology experiments were dark adapted for at least 2 hours, and
663 the retinas were isolated under infrared light following procedures approved by the Administrative
664 Panel on Laboratory Animal Care at the University of Washington. Retinas were continuously
665 superfused (~8 mL/min) with oxygenated (95% O₂, 5% CO₂) bicarbonate-buffered Ames solution
666 (Sigma) maintained at 25°C–28°C.

667 Recordings were conducted in a flat-mount preparation with photoreceptors facing down. Bipolar
668 cells were patched at the axon terminals. To access bipolar cell terminals for recording, small
669 groups of ganglion cells were suctioned off the top of the retina to expose the inner plexiform
670 layer. Terminals of RBC1 bipolar cells could be targeted for recording using only infrared
671 illumination, whereas RBC2 terminals, which were not easily visible without fluorescence imaging,
672 were targeted using a custom-built two-photon microscope. As a result, measuring rod-mediated
673 responses in RBC2 was unfeasible due to the compromise of rod responses by two-photon
674 imaging.

675 Whole-cell voltage-clamp recordings were obtained using patch pipettes filled with a Cs⁺-based
676 internal solution. This internal solution also included Alexa Fluor 594, which was used for two-
677 photon imaging of each cell after recording to confirm its type by morphology. To isolate excitatory
678 postsynaptic currents, we voltage-clamped cells near the reversal potential for chloride-mediated
679 conductances (~-60 mV). In addition, to block inhibitory synaptic transmission, we added the

680 GABAA receptor antagonist gabazine (20 μ M), the GABAC receptor antagonist TPMPA (50 μ M),
681 and the glycine receptor antagonist strychnine (3 μ M) to the superfusion solution. In experiments
682 in which mGluR6-mediated input was blocked, the mGluR6 receptor agonist APB (10 μ M) was
683 also added to the superfusion.

684 Light from blue or red light-emitting diodes (LEDs, peak output = 470 nm and 640 nm respectively)
685 was delivered to the recording chamber via fiber optic cable positioned beneath the microscope's
686 condenser lens. The light uniformly illuminated a circular area through an aperture 0.5 mm in
687 diameter centered on the recorded cell. Protocols for light stimulation were designed to either
688 activate rods only (using the blue LED) or both rods and cones (using the red LED).

689 **EM data acquisition, reconstruction, and annotation**

690 Dissected retinal tissues from wild type adult zebrafish were immediately transferred into a 1.5-
691 ml tube with the fixative (4% glutaraldehyde in 0.1M cacodylate buffer [pH7.4]) and incubated
692 overnight on a shaker at RT. Subsequently, the tissue was washed three times in 0.1 M
693 cacodylate buffer (pH7.4) and incubated in a solution containing 1.5% potassium ferrocyanide
694 and 2% osmium tetroxide (OsO₄) in 0.1 M cacodylate buffer [0.66% lead in 0.03 M aspartic acid
695 (pH 5.5)] for 1 hour. After washing, the tissue was placed in a freshly made thiocarbohydrazide
696 (TCH) solution (0.1 g of TCH in 10 ml of double-distilled H₂O heated to 600°C for 1 hour) for 20
697 min at RT. After another rinse, at RT, the tissue was incubated in 2% OsO₄ for 30 min at RT. The
698 samples were rinsed again and stained en bloc in 1% uranyl acetate overnight at 40°C, washed,
699 and stained with Walton's lead aspartate for 30 min. After a final wash, the retinal pieces were
700 dehydrated in a graded ice-cold alcohol series and placed in propylene oxide at RT for 10 min.
701 Last, the sample was embedded in Durcupan resin. Semithin sections (0.5 to 1 μ m thick) were
702 cut and stained with toluidine blue, until the fiducial marks (box) in the ganglion cell layer (GCL)
703 appeared. The block was then trimmed and mounted in a serial block-face scanning electron
704 microscope (GATAN/Zeiss, 3View). Serial sections were cut at a thickness of 70 nm and imaged

705 at an xy resolution of 7 nm. Six tiles, each about 40 μ m by 40 μ m with an overlap of about 10%,
706 covering from the outer nucleus layer to the ganglion cell layer in a side view was obtained. Retinal
707 location was not recorded. The image stacks were concatenated and aligned using TrakEM2
708 (NIH). Neurons were traced or painted using the tracing and painting tools in TrakEM2.

709 **Statistics**

710 Mann-Whitney U test was used to determine the *p*-value for comparing dendritic field sizes.

711

712 **DATA AVAILABILITY**

713 Computational scripts detailing scRNA-seq analysis reported in this paper are available at
714 <https://github.com/shekharlab/>

715 ZebrafishBC. We have also provided R markdown (Rmd) files that show step-by-step
716 reproduction of the key results at <https://github.com/shekharlab/ZebrafishBC>. The raw and
717 processed scRNA-seq data reported in this paper was obtained from the Gene Expression
718 Omnibus (GEO) entry GSE237215 (subseries GSE237214).

719

720

721

722

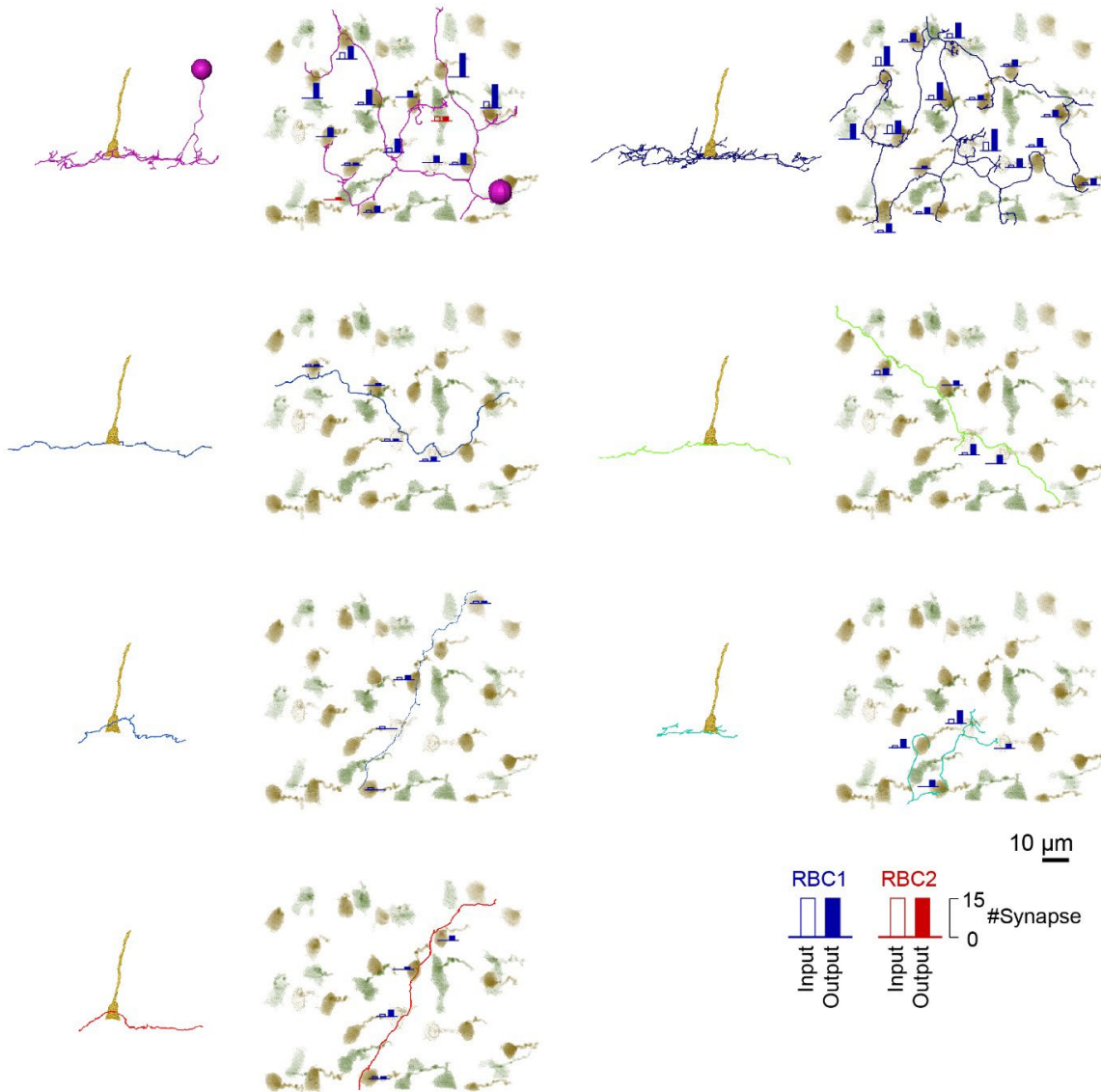
723

724

725

Figure S4

Monostratifying-AC with reciprocal synapses
(A17-like)



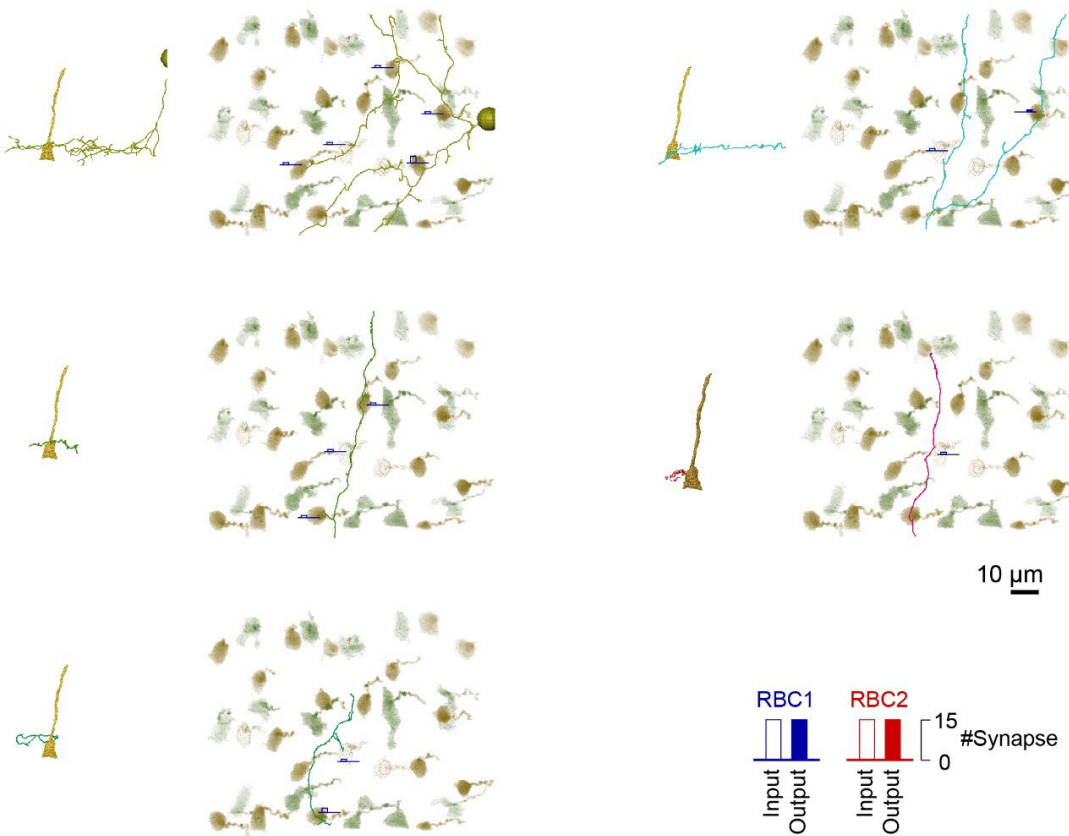
726

727 **Figure S4. Gallery of mono-stratifying AC making reciprocal synapses with RBC1**

728 *En face and side views of individual cells or processes. The numbers of input (open bar) and*
729 *output (closed bar) synapses with each RBC1 (blue) and RBC2 (red) terminal are indicated as*
730 *the height of the bars.*

Figure S5

Monostratifying-AC without reciprocal synapses



731

732 **Figure S5. Gallery of mono-stratifying AC without reciprocal synapses with RBC1**

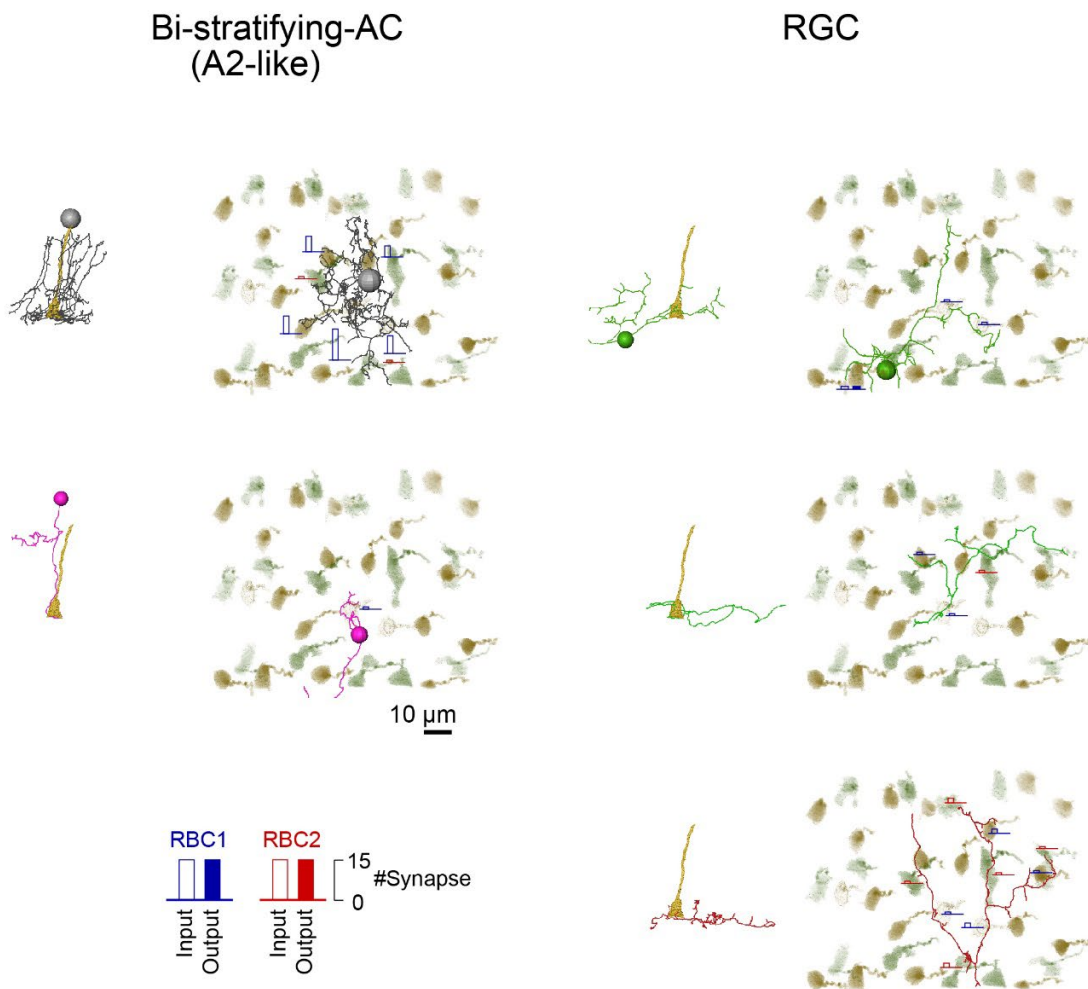
733 *En face and side views of individual cells. The numbers of input (open bar) and output (closed
734 bar) synapses with each RBC1 (blue) and RBC2 (red) terminal are indicated as the height of the
735 bars.*

736

737

738

Figure S6



739

740 **Figure S6. Gallery of bi-stratifying AC and RGC contacted to RBC1**

741 *En face and side views of individual cells. The numbers of input (open bar) and output (closed*
742 *bar) synapses with each RBC1 (blue) and RBC2 (red) terminal are indicated as the height of the*
743 *bars.*

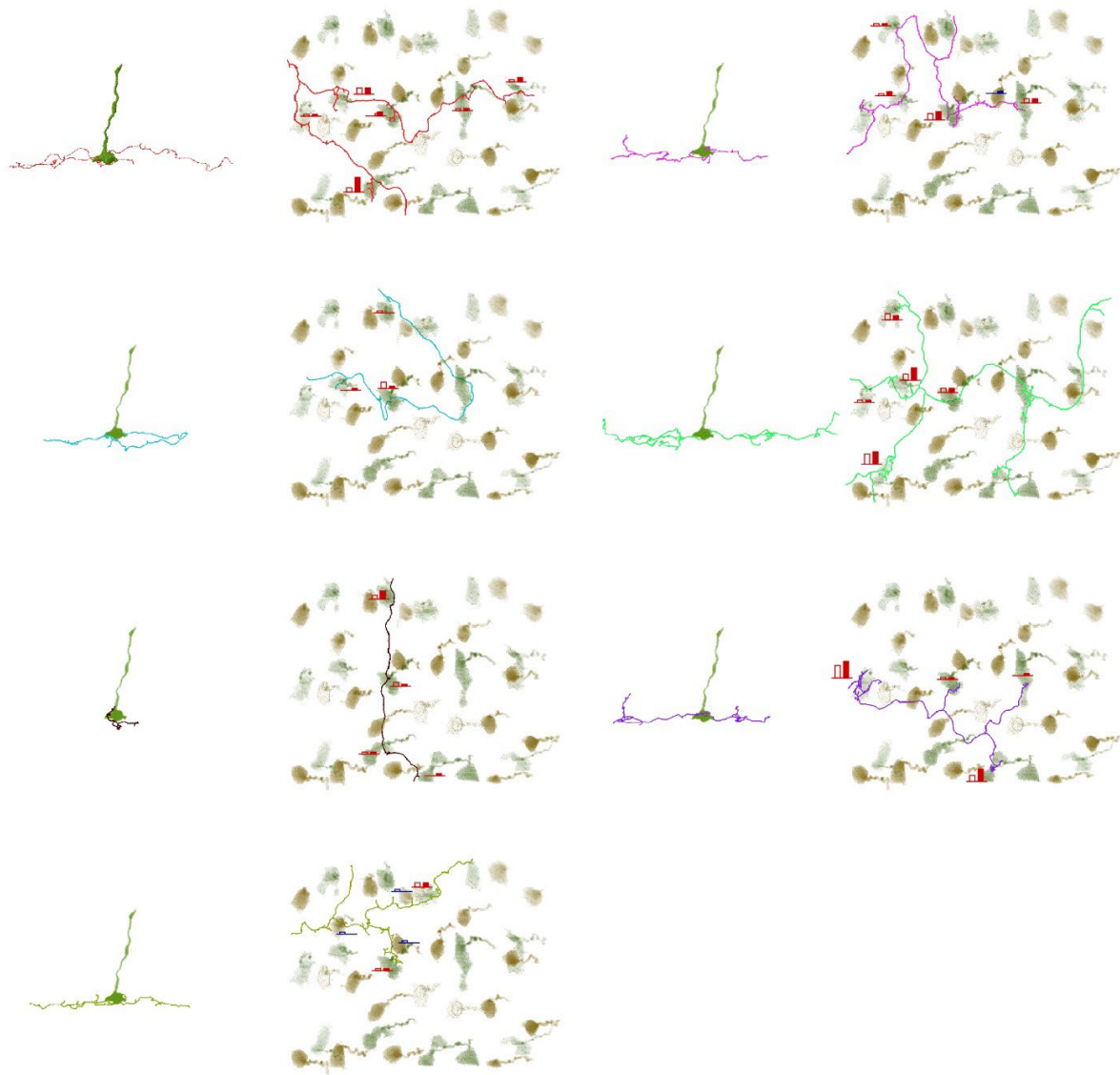
744

745

746

Figure S7

Monostratifying-AC with reciprocal synapses



Monostratifying-AC without reciprocal synapses

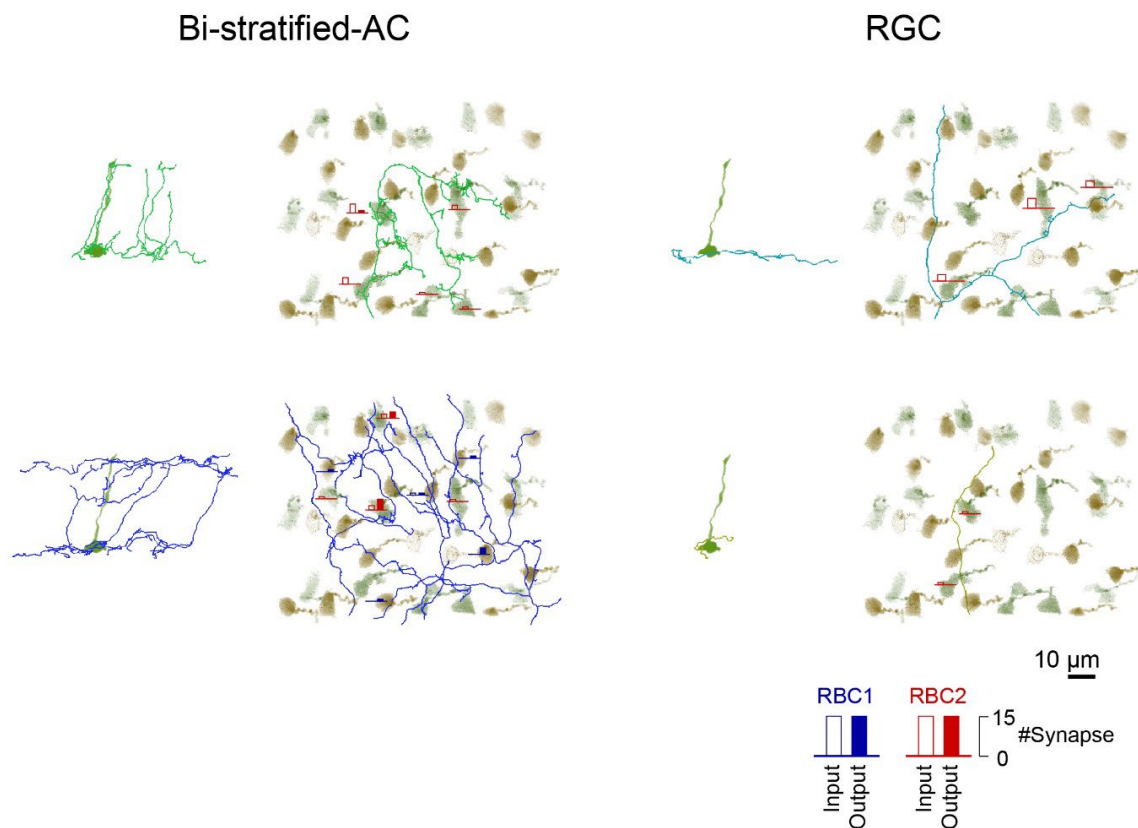


748 **Figure S7. Gallery of mono-stratifying AC connected to RBC2**

749 *En face and side views of individual cells. The numbers of input (open bar) and output (closed*
750 *bar) synapses with each RBC1 (blue) and RBC2 (red) terminal are indicated as the height of the*
751 *bars.*

752

Figure S8



753

754 **Figure S8. Gallery of bi-stratifying AC and RGC connected to RBC2**

755 *En face and side views of individual cells. The numbers of input (open bar) and output (closed*
756 *bar) synapses with each RBC1 (blue) and RBC2 (red) terminal are indicated as the height of the*
757 *bars.*

758

759 **REFERENCES**

- 760 1. Morshedian, A. & Fain, G. L. The evolution of rod photoreceptors. *Philos. Trans. R. Soc. B Biol. Sci.*
761 **372**, 20160074 (2017).
- 762 2. Bloomfield, S. A. & Dacheux, R. F. Rod Vision: Pathways and Processing in the Mammalian Retina.
763 *Prog. Retin. Eye Res.* **20**, 351–384 (2001).
- 764 3. Field, G. D., Sampath, A. P. & Rieke, F. RETINAL PROCESSING NEAR ABSOLUTE THRESHOLD: From
765 Behavior to Mechanism. *Annu. Rev. Physiol.* **67**, 491–514 (2005).
- 766 4. Grimes, W. N., Songco-Aguas, A. & Rieke, F. Parallel Processing of Rod and Cone Signals: Retinal
767 Function and Human Perception. *Annu. Rev. Vis. Sci.* **4**, 123–141 (2018).
- 768 5. Strettoi, E. 1.11 - Mammalian Rod Pathways. in *The Senses: A Comprehensive Reference* (eds.
769 Masland, R. H. et al.) 303–311 (Academic Press, 2008). doi:10.1016/B978-012370880-9.00266-8.
- 770 6. Wu, S. M. Synaptic Organization of the Vertebrate Retina: General Principles and Species-Specific
771 Variations: The Friedenwald Lecture. *Invest. Ophthalmol. Vis. Sci.* **51**, 1264–1274 (2010).
- 772 7. Thoreson, W. B. & Dacey, D. M. Diverse Cell Types, Circuits, and Mechanisms for Color Vision in the
773 Vertebrate Retina. *Physiol. Rev.* **99**, 1527–1573 (2019).
- 774 8. Behrens, C., Schubert, T., Haverkamp, S., Euler, T. & Berens, P. Connectivity map of bipolar cells and
775 photoreceptors in the mouse retina. *eLife* **5**, e20041 (2016).
- 776 9. Baylor, D. A., Lamb, T. D. & Yau, K. W. Responses of retinal rods to single photons. *J. Physiol.* **288**,
777 613–634 (1979).
- 778 10. Baylor, D. A., Nunn, B. J. & Schnapf, J. L. The photocurrent, noise and spectral sensitivity of rods of
779 the monkey *Macaca fascicularis*. *J. Physiol.* **357**, 575–607 (1984).
- 780 11. Field, G. D. & Rieke, F. Nonlinear Signal Transfer from Mouse Rods to Bipolar Cells and Implications
781 for Visual Sensitivity. *Neuron* **34**, 773–785 (2002).

782 12. Field, G. D. & Rieke, F. Mechanisms regulating variability of the single photon responses of
783 mammalian rod photoreceptors. *Neuron* **35**, 733–747 (2002).

784 13. Ingram, N. T., Sampath, A. P. & Fain, G. L. Why are rods more sensitive than cones? *J. Physiol.* **594**,
785 5415–5426 (2016).

786 14. Yang, X.-L. & Wu, S. M. Response Sensitivity and Voltage Gain of the Rod- and Cone-Bipolar Cell
787 Synapses in Dark-Adapted Tiger Salamander Retina. *J. Neurophysiol.* **78**, 2662–2673 (1997).

788 15. Kolb, H. & Famiglietti, E. V. Rod and Cone Pathways in the Inner Plexiform Layer of Cat Retina.
789 *Science* **186**, 47–49 (1974).

790 16. Strettoi, E., Masri, R. A. & Grünert, U. All amacrine cells in the primate fovea contribute to photopic
791 vision. *Sci. Rep.* **8**, 16429 (2018).

792 17. Lee, S. C. S., Martin, P. R. & Grünert, U. Topography of Neurons in the Rod Pathway of Human
793 Retina. *Invest. Ophthalmol. Vis. Sci.* **60**, 2848–2859 (2019).

794 18. Tsukamoto, Y., Morigiwa, K., Ueda, M. & Sterling, P. Microcircuits for Night Vision in Mouse Retina.
795 *J. Neurosci.* **21**, 8616–8623 (2001).

796 19. Kolb, H. & Nelson, R. Rod pathways in the retina of the cat. *Vision Res.* **23**, 301–312 (1983).

797 20. Dacheux, R. F. & Raviola, E. The rod pathway in the rabbit retina: a depolarizing bipolar and
798 amacrine cell. *J. Neurosci.* **6**, 331–345 (1986).

799 21. Freed, M. A., Smith, R. G. & Sterling, P. Rod bipolar array in the cat retina: pattern of input from rods
800 and GABA-accumulating amacrine cells. *J. Comp. Neurol.* **266**, 445–455 (1987).

801 22. Joselevitch, C. & Kamermans, M. Retinal parallel pathways: Seeing with our inner fish. *Vision Res.*
802 **49**, 943–959 (2009).

803 23. Franke, K. *et al.* Inhibition decorrelates visual feature representations in the inner retina. *Nature*
804 **542**, 439–444 (2017).

805 24. Ghosh, K. K., Bujan, S., Haverkamp, S., Feigenspan, A. & Wässle, H. Types of bipolar cells in the
806 mouse retina. *J. Comp. Neurol.* **469**, 70–82 (2004).

807 25. Grünert, U. & Martin, P. R. Cell types and cell circuits in human and non-human primate retina.
808 *Prog. Retin. Eye Res.* 100844 (2020) doi:10.1016/j.preteyeres.2020.100844.

809 26. Peng, Y.-R. *et al.* Molecular Classification and Comparative Taxonomics of Foveal and Peripheral
810 Cells in Primate Retina. *Cell* **176**, 1222-1237.e22 (2019).

811 27. Shekhar, K. *et al.* Comprehensive Classification of Retinal Bipolar Neurons by Single-Cell
812 Transcriptomics. *Cell* **166**, 1308-1323.e30 (2016).

813 28. Masland, R. H. The neuronal organization of the retina. *Neuron* **76**, 266–80 (2012).

814 29. Hahn, J. *et al.* Evolution of neuronal cell classes and types in the vertebrate retina.
815 2023.04.07.536039 Preprint at <https://doi.org/10.1101/2023.04.07.536039> (2023).

816 30. Strettoi, E., Dacheux, R. F. & Raviola, E. Synaptic connections of rod bipolar cells in the inner
817 plexiform layer of the rabbit retina. *J. Comp. Neurol.* **295**, 449–466 (1990).

818 31. Zhang, C., Hellevik, A., Takeuchi, S. & Wong, R. O. Hierarchical partner selection shapes rod-cone
819 pathway specificity in the inner retina. *iScience* **25**, 105032 (2022).

820 32. Strettoi, E., Raviola, E. & Dacheux, R. F. Synaptic connections of the narrow-field, bistratified rod
821 amacrine cell (All) in the rabbit retina. *J. Comp. Neurol.* **325**, 152–168 (1992).

822 33. Dunn, F. A. & Rieke, F. Single-Photon Absorptions Evoke Synaptic Depression in the Retina to Extend
823 the Operational Range of Rod Vision. *Neuron* **57**, 894–904 (2008).

824 34. Grimes, W. N., Hoon, M., Briggman, K. L., Wong, R. O. & Rieke, F. Cross-synaptic synchrony and
825 transmission of signal and noise across the mouse retina. *eLife* **3**, e03892 (2014).

826 35. Pang, J.-J., Gao, F. & Wu, S. M. Light-evoked current responses in rod bipolar cells, cone depolarizing
827 bipolar cells and All amacrine cells in dark-adapted mouse retina. *J. Physiol.* **558**, 897–912 (2004).

828 36. Demb, J. B. & Singer, J. H. Intrinsic properties and functional circuitry of the All amacrine cell. *Vis. Neurosci.* **29**, 51–60 (2012).

830 37. Strettoi, E., Dacheux, R. F. & Raviola, E. Cone bipolar cells as interneurons in the rod, pathway of the rabbit retina. *J. Comp. Neurol.* **347**, 139–149 (1994).

832 38. Vitorino, M. *et al.* Vsx2 in the zebrafish retina: restricted lineages through derepression. *Neural Develop.* **4**, 14 (2009).

834 39. Križaj, D., Cordeiro, S. & Strauß, O. Retinal TRP channels: Cell-type-specific regulators of retinal homeostasis and multimodal integration. *Prog. Retin. Eye Res.* **92**, 101114 (2023).

836 40. Becht, E. *et al.* Dimensionality reduction for visualizing single-cell data using UMAP. *Nat. Biotechnol.* **37**, 38–44 (2019).

838 41. Wässle, H., Yamashita, M., Greferath, U., Grünert, U. & Müller, F. The rod bipolar cell of the mammalian retina. *Vis. Neurosci.* **7**, 99–112 (1991).

840 42. Wässle, H., Puller, C., Müller, F. & Haverkamp, S. Cone Contacts, Mosaics, and Territories of Bipolar Cells in the Mouse Retina. *J. Neurosci.* **29**, 106–117 (2009).

842 43. Choi, H. M. T. *et al.* Third-generation *in situ* hybridization chain reaction: multiplexed, quantitative, sensitive, versatile, robust. *Development* **145**, dev165753 (2018).

844 44. Vihtelic, T. S., Doro, C. J. & Hyde, D. R. Cloning and characterization of six zebrafish photoreceptor opsins and immunolocalization of their corresponding proteins. *Vis. Neurosci.* **16**, 571–585 (1999).

847 45. Chinen, A., Hamaoka, T., Yamada, Y. & Kawamura, S. Gene Duplication and Spectral Diversification of Cone Visual Pigments of Zebrafish. *Genetics* **163**, 663–675 (2003).

849 46. Sandell, J. H., Masland, R. H., Raviola, E. & Dacheux, R. F. Connections of indoleamine-accumulating cells in the rabbit retina. *J. Comp. Neurol.* **283**, 303–313 (1989).

851 47. Grimes, W. N., Zhang, J., Graydon, C. W., Kachar, B. & Diamond, J. S. Retinal parallel processors:
852 more than 100 independent microcircuits operate within a single interneuron. *Neuron* **65**, 873–885
853 (2010).

854 48. Marc, R. E., Anderson, J. R., Jones, B. W., Sigulinsky, C. L. & Lauritzen, J. S. The All amacrine cell
855 connectome: a dense network hub. *Front. Neural Circuits* **8**, (2014).

856 49. Gamlin, C. R., Zhang, C., Dyer, M. A. & Wong, R. O. L. Distinct Developmental Mechanisms Act
857 Independently to Shape Biased Synaptic Divergence from an Inhibitory Neuron. *Curr. Biol. CB* **30**,
858 1258-1268.e2 (2020).

859 50. Tsukamoto, Y. & Omi, N. Functional allocation of synaptic contacts in microcircuits from rods via rod
860 bipolar to All amacrine cells in the mouse retina. *J. Comp. Neurol.* **521**, 3541–3555 (2013).

861 51. Li, Y. N., Tsujimura, T., Kawamura, S. & Dowling, J. E. Bipolar Cell-Photoreceptor Connectivity in the
862 Zebrafish (*Danio rerio*) Retina. *J. Comp. Neurol.* **520**, 3786–3802 (2012).

863 52. Zimmermann, M. J. Y. *et al.* Zebrafish Differentially Process Color across Visual Space to Match
864 Natural Scenes. *Curr. Biol. CB* **28**, 2018-2032.e5 (2018).

865 53. Zhou, M. *et al.* Zebrafish Retinal Ganglion Cells Asymmetrically Encode Spectral and Temporal
866 Information across Visual Space. *Curr. Biol.* **30**, 2927-2942.e7 (2020).

867 54. Yoshimatsu, T., Schröder, C., Nevala, N. E., Berens, P. & Baden, T. Fovea-like Photoreceptor
868 Specializations Underlie Single UV Cone Driven Prey-Capture Behavior in Zebrafish. *Neuron* **107**,
869 320-337.e6 (2020).

870 55. Schröder, C., Oesterle, J., Berens, P., Yoshimatsu, T. & Baden, T. Distinct synaptic transfer functions
871 in same-type photoreceptors. *eLife* **10**, e67851 (2021).

872 56. Yan, W. *et al.* Cell Atlas of The Human Fovea and Peripheral Retina. *Sci. Rep.* **10**, 9802 (2020).

873 57. Günther, A. *et al.* Double Cones and the Diverse Connectivity of Photoreceptors and Bipolar Cells in
874 an Avian Retina. *J. Neurosci.* **41**, 5015–5028 (2021).

875 58. Yamagata, M., Yan, W. & Sanes, J. R. A cell atlas of the chick retina based on single-cell
876 transcriptomics. *eLife* **10**, e63907 (2021).

877 59. Baden, T. & Osorio, D. The Retinal Basis of Vertebrate Color Vision. *Annu. Rev. Vis. Sci.* **5**, 177–200
878 (2019).

879 60. Lamb, T. D. Evolution of phototransduction, vertebrate photoreceptors and retina. *Prog. Retin. Eye*
880 *Res.* **36**, 52–119 (2013).

881 61. Sherry, D. M. & Yazulla, S. Goldfish bipolar cells and axon terminal patterns: A Golgi study. *J. Comp.*
882 *Neurol.* **329**, 188–200 (1993).

883 62. Behrens, U. D., Borde, J., Mack, A. F. & Wagner, H.-J. Distribution of phosphorylated protein kinase C
884 alpha in goldfish retinal bipolar synaptic terminals: control by state of adaptation and
885 pharmacological treatment. *Cell Tissue Res.* **327**, 209–220 (2007).

886 63. Pang, J.-J., Gao, F. & Wu, S. M. Stratum-by-stratum projection of light response attributes by retinal
887 bipolar cells of *Ambystoma*. *J. Physiol.* **558**, 249–262 (2004).

888 64. Balaji, V. *et al.* Immunohistochemical characterization of bipolar cells in four distantly related avian
889 species. *J. Comp. Neurol.* **531**, 561–581 (2023).

890 65. Caminos, E., Velasco, A., Jarrín, M., Aijón, J. & Lara, J. M. Protein kinase C-like immunoreactive cells
891 in embryo and adult chicken retinas. *Dev. Brain Res.* **118**, 227–230 (1999).

892 66. Frederiksen, R., Fain, G. L. & Sampath, A. P. A hyperpolarizing rod bipolar cell in the sea lamprey,
893 *Petromyzon marinus*. *J. Exp. Biol.* **225**, jeb243949 (2022).

894 67. Tsukamoto, Y. & Omi, N. Classification of Mouse Retinal Bipolar Cells: Type-Specific Connectivity
895 with Special Reference to Rod-Driven All Amacrine Pathways. *Front. Neuroanat.* **11**, 92 (2017).

896 68. Wong, K. Y., Cohen, E. D. & Dowling, J. E. Retinal Bipolar Cell Input Mechanisms in Giant Danio. II.
897 Patch-Clamp Analysis of on Bipolar Cells. *J. Neurophysiol.* **93**, 94–107 (2005).

898 69. Yoshimatsu, T. *et al.* Ancestral circuits for vertebrate color vision emerge at the first retinal synapse.
899 *Sci. Adv.* **7**, eabj6815 (2021).

900 70. Ishida, A. T., Stell, W. K. & Lightfoot, D. O. Rod and cone inputs to bipolar cells in goldfish retina. *J.*
901 *Comp. Neurol.* **191**, 315–335 (1980).

902 71. Connaughton, V. P. & Nelson, R. Axonal stratification patterns and glutamate-gated conductance
903 mechanisms in zebrafish retinal bipolar cells. *J. Physiol.* **524 Pt 1**, 135–46 (2000).

904 72. Joselevitch, C. & Kamermans, M. Interaction between rod and cone inputs in mixed-input bipolar
905 cells in goldfish retina. *J. Neurosci. Res.* **85**, 1579–1591 (2007).

906 73. Pang, J.-J. *et al.* Direct rod input to cone BCs and direct cone input to rod BCs challenge the
907 traditional view of mammalian BC circuitry. *Proc. Natl. Acad. Sci.* **107**, 395–400 (2010).

908 74. Pang, J.-J., Yang, Z., Jacoby, R. A. & Wu, S. M. Cone synapses in mammalian retinal rod bipolar cells.
909 *J. Comp. Neurol.* **526**, 1896–1909 (2018).

910 75. Whitaker, C. M., Nobles, G., Ishibashi, M. & Massey, S. C. Rod and Cone Connections With Bipolar
911 Cells in the Rabbit Retina. *Front. Cell. Neurosci.* **15**, 662329 (2021).

912 76. Carter-Dawson, L. D. & LaVail, M. M. Rods and cones in the mouse retina. I. Structural analysis using
913 light and electron microscopy. *J. Comp. Neurol.* **188**, 245–262 (1979).

914 77. Famiglietti, E. V. & Sharpe, S. J. Regional topography of rod and immunocytochemically
915 characterized ‘blue’ and ‘green’ cone photoreceptors in rabbit retina. *Vis. Neurosci.* **12**, 1151–1175
916 (1995).

917 78. Kimura, Y., Satou, C. & Higashijima, S. V2a and V2b neurons are generated by the final divisions of
918 pair-producing progenitors in the zebrafish spinal cord. *Development* **135**, 3001–3005 (2008).

919 79. Randlett, O. *et al.* Cellular requirements for building a retinal neuropil. *Cell Rep.* **3**, 282–290 (2013).

920 80. Suzuki, S. C. *et al.* Cone photoreceptor types in zebrafish are generated by symmetric terminal
921 divisions of dedicated precursors. *Proc. Natl. Acad. Sci.* **110**, 15109–15114 (2013).

922 81. Kölsch, Y. *et al.* Molecular classification of zebrafish retinal ganglion cells links genes to cell types to
923 behavior. *Neuron* **109**, 645–662.e9 (2021).

924 82. La Manno, G. *et al.* RNA velocity of single cells. *Nature* **560**, 494–498 (2018).

925 83. Hafemeister, C. & Satija, R. Normalization and variance stabilization of single-cell RNA-seq data
926 using regularized negative binomial regression. *Genome Biol.* **20**, 296 (2019).

927 84. Bernardos, R. L., Barthel, L. K., Meyers, J. R. & Raymond, P. A. Late-Stage Neuronal Progenitors in
928 the Retina Are Radial Müller Glia That Function as Retinal Stem Cells. *J. Neurosci.* **27**, 7028–7040
929 (2007).

930 85. Hörnberg, H. *et al.* RNA-binding protein Hermes/RBPMS inversely affects synapse density and axon
931 arbor formation in retinal ganglion cells in vivo. *J. Neurosci. Off. J. Soc. Neurosci.* **33**, 10384–10395
932 (2013).

933 86. Sandell, J. H., Martin, S. C. & Heinrich, G. The development of GABA immunoreactivity in the retina
934 of the zebrafish (*Brachydanio rerio*). *J. Comp. Neurol.* **345**, 596–601 (1994).

935 87. Abalo, X. M. *et al.* Circadian regulation of phosphodiesterase 6 genes in zebrafish differs between
936 cones and rods: Implications for photopic and scotopic vision. *Vision Res.* **166**, 43–51 (2020).

937 88. Kolosov, D., Bui, P., Chasiotis, H. & Kelly, S. P. Claudins in teleost fishes. *Tissue Barriers* **1**, e25391
938 (2013).

939 89. Kwan, K. M. *et al.* The Tol2kit: A multisite gateway-based construction kit for Tol2 transposon
940 transgenesis constructs. *Dev. Dyn.* **236**, 3088–3099 (2007).

941 90. Morris, A. C., Scholz, T. L., Brockerhoff, S. E. & Fadool, J. M. Genetic Dissection Reveals Two Separate
942 Pathways for Rod and Cone Regeneration in the Teleost Retina. *Dev. Neurobiol.* **68**, 605–619 (2008).

943 91. Huang, Y.-Y., Haug, M. F., Gesemann, M. & Neuhauss, S. C. F. Novel Expression Patterns of
944 Metabotropic Glutamate Receptor 6 in the Zebrafish Nervous System. *PLOS ONE* **7**, e35256 (2012).

945